DISEASES AND DISORDERS

Cardiolipin content controls mitochondrial coupling and energetic efficiency in muscle

Alexandre Prola[1,2,3], Jordan Blondelle[1,2,3]*, Aymeline Vandestienne[1,2,3]*, Jérôme Piquereau[4], Raphaël G. P. Denis[5], Stéphane Guyot[6], Hadrien Chauvin[1,2,3], Arnaud Mourier[7], Marie Maurer[1,2,3], Céline Henry[8], Nahed Khadhraoui[1,2,3], Cindy Gallerne[1,2,3], Thibaut Molinié[7], Guillaume Courtin[1,2,3], Laurent Guillaud[1,2,3], Mélanie Gressette[4], Audrey Solgadi[9], Florent Dumont[9], Julien Castel[5], Julien Ternacle[10], Jean Demarquoy[6], Alexandra Malgoyre[11,12], Nathalie Koulmann[11,12,13], Geneviève Derumeaux[10], Marie-France Giraud[7,8], Frédéric Joubert[12], Vladimir Veksler[4], Serge Luquet[5], Frédéric Relaix[1,2,3†], Laurent Tiret[1,2,3†], Fanny Pilot-Storck[1,2,3†]

Copyright © 2021 The Authors, some rights reserved; exclusive licensee American Association for the Advancement of Science. No claim to original U.S. Government Works. Distributed under a Creative Commons Attribution NonCommercial License 4.0 (CC BY-NC).

Unbalanced energy partitioning participates in the rise of obesity, a major public health concern in many countries. Increasing basal energy expenditure has been proposed as a strategy to fight obesity yet raises efficiency and safety concerns. Here, we show that mice deficient for a muscle-specific enzyme of very-long-chain fatty acid synthesis display increased basal energy expenditure and protection against high-fat diet–induced obesity. Mechanistically, muscle-specific modulation of the very-long-chain fatty acid pathway was associated with a reduced content of the inner mitochondrial membrane phospholipid cardiolipin and a blunted coupling efficiency between the respiratory chain and adenosine 5′-triphosphate (ATP) synthase, which was restored by cardiolipin enrichment. Our study reveals that selective increase of lipid oxidative capacities in skeletal muscle, through the cardiolipin-dependent lowering of mitochondrial ATP production, provides an effective option against obesity at the whole-body level.

INTRODUCTION

Increased food intake and prevailing sedentary activities cause a positive energy balance, leading to an unprecedented obesity epidemic, which is nowadays rising at an alarming pace (*1*). Obesity is not only associated with many other comorbidities including metabolic disorders (i.e., insulin resistance, metabolic syndrome, and diabetes) but also cancer, cardiovascular, or emerging infectious diseases, increasing therefore the risk of mortality (*2*–*5*). Beneficial effects of regular exercise to counter obesity and related diseases have been demonstrated but, unfortunately, are hampered by poor compliance and low energy expenditure (*6*, *7*). In this context, increasing basal energy expenditure, independently of exercise, might be an interesting strategy to prevent obesity-related complications (*8*). Basal energy production relies almost entirely on the mitochondrial function ensuring the efficient production of adenosine 5′-triphosphate (ATP) from energetic substrates through the oxidative phosphorylation (OXPHOS) process, which takes place in the inner mitochondrial membrane (IMM) and couples the generation of a transmembrane gradient of protons by the respiratory chain to the adenosine 5′-diphosphate (ADP) phosphorylation by ATP synthase (*9*). Any reduction in OXPHOS coupling decreases energetic yield and may lead to increased expenditure of energy substrates to counteract low ATP productivity (*8*). Mitochondrial organization and function is an active field of research, and further insights into the physiological mechanisms that regulate mitochondrial coupling efficiency are a prerequisite for the identification of innovative therapeutic strategies. A notable feature of mitochondria stands in its highly specialized structure. In particular, folding of the IMM into packed cristae is thought to allow optimized organization of respiratory complexes and ATP synthase for efficient ATP production (*10*). Tight folding of such an extended membrane is not a classical organization of lipid bilayer sheets and involves a dedicated lipid composition. Notably, the IMM contains the specific four-acyl chain phospholipid cardiolipin, which has been shown to favor proper cristae folding, respiratory chain, and ATP synthase function (*11*–*14*). Modulation of cardiolipin composition is likely one of the levers used by cells to optimize energetic yield in highly ATP-demanding tissues. Mutations in tafazzin, a cardiolipin-remodeling enzyme that tends to homogenize cardiolipin chains to linoleic acyls (C18:2) in heart and skeletal muscle, hamper mitochondrial function and are associated with cardiomyopathy and myopathy (*15*, *16*). Whether other lipid-based mechanisms are involved in optimizing ATP production in these tissues remains to be deciphered. Fatty acids with 18 carbons or more are synthesized by the very-long-chain fatty acid (VLCFA) enzymatic complex in the endoplasmic reticulum membrane through a four-step cycle (*17*, *18*). The first step of elongation is accomplished by fatty acid elongases encoded by seven different *ELOVL* genes with overlapping expression profiles, and the second and fourth steps are under the control of unique genes (*18*). The third step is catalyzed by 3-hydroxyacyl–coenzyme A (CoA) dehydratase (HACD) proteins, which are encoded by four different genes (*17*, *19*). Notably,

[1]Université Paris-Est Créteil, INSERM, IMRB, Team Relaix, F-94010 Créteil, France. [2]EnvA, IMRB, F-94700 Maisons-Alfort, France. [3]EFS, IMRB, F-94010 Créteil, France. [4]UMR-S 1180, INSERM, Université Paris-Sud, Université Paris-Saclay, F-92296 Châtenay-Malabry, France. [5]Université de Paris, BFA, UMR 8251, CNRS, F-75014 Paris, France. [6]Université Bourgogne Franche-Comté, AgroSup Dijon, PAM UMR A 02.102, F-21000 Dijon, France. [7]Université Bordeaux, CNRS, IBGC, UMR 5095, F-33000 Bordeaux, France. [8]PAPPSO, Université Paris-Saclay, INRAE, AgroParisTech, Micalis Institute, F-78350 Jouy-en-Josas, France. [9]UMS IPSIT, Université Paris-Saclay, F-92296 Châtenay-Malabry, France. [10]Université Paris-Est Créteil, INSERM, IMRB, Team Derumeaux, F-94010 Creteil, France. [11]Département Environnements Opérationnels, Unité de Physiologie des Exercices et Activités en Conditions Extrêmes, Institut de Recherche Biomédicale des Armées, F-91220 Brétigny-Sur-Orge, France. [12]LBEPS, Université Evry, IRBA, Université Paris-Saclay, F-91025 Evry, France. [13]École du Val de Grâce, Place Alphonse Laveran, F-75005 Paris, France.
*These authors contributed equally to this work.
†Corresponding author. Email: fanny.storck@vet-alfort.fr (F.P.-S.); laurent.tiret@vet-alfort.fr (L.T.); frederic.relaix@inserm.fr (F.R.)

Downloaded from http://advances.sciencemag.org/ on January 26, 2021

expression of the *HACD1* active isoform is restricted to the heart and skeletal muscle, in which it promotes efficient myoblast fusion during muscle development (*20*). While *HACD1* deficiency leads to congenital myopathies in humans, dogs, and mice sharing an early and stable reduction in muscle mass and strength (*20*–*23*), the metabolic consequences of *HACD1* deficiency remained to be deciphered.

Counterintuitively, we describe here that *Hacd1*-deficient mice stay lean throughout life and that they are protected against diet-induced obesity. An in-depth analysis of their metabolic features uncovers an increased expenditure of energy substrates by the skeletal muscle alone, independently of locomotor activity and excluding the heart, whose function remains unchanged. Upon *Hacd1* deficiency, mitochondria of skeletal muscle display a reduced coupling between substrates oxidation and ADP phosphorylation by the ATP synthase, responsible for higher energy substrate consumption. Skeletal muscle mitochondria of *Hacd1*-deficient mice exhibit modified cristae and reduced cardiolipin content, and cardiolipin enrichment fully rescues respiratory coupling efficiency in isolated mitochondria.

Together, our data reveal that skeletal muscle benefits from a specific mechanism involving the VLCFA elongation cycle to ensure optimized ATP production and that cardiolipin content in this tissue influences energy balance at the body level.

RESULTS

Genetic invalidation of *Hacd1* leads to protection against diet-induced obesity

Hacd1–knockout (KO) mice present mild myopathic features characterized by a congenital reduction in muscle mass (*20*) and reduced spontaneous locomotor activity, both in distance and speed (Fig. 1A and fig. S1A). Unexpectedly, *Hacd1*-KO mice did not gain more weight but remained leaner than wild-type (WT) mice throughout their life span (Fig. 1, B and C). To investigate whether this observation could be related to a difference in energy homeostasis, we challenged *Hacd1*-KO mice with high-fat diet (HFD). As expected, WT mice regularly gained weight and became obese following a 2-month HFD (Fig. 1, C and D). On the contrary, *Hacd1*-KO mice showed only moderate weight gain, thus escaping obesity (Fig. 1, C and D). Accordingly, *Hacd1*-KO mice were more tolerant to a glucose overload than WT mice after HFD (Fig. 1, E and F). Furthermore, we found a prominent reduction in fat accumulation in *Hacd1*-KO mice after HFD compared to WT mice. In particular, we observed a blunted increase in white adipose tissue (WAT) weight (Fig. 1G, fig. S1B, and table S1), while a lesser amount of liver steatosis occurred in *Hacd1*-KO mice as compared with WT mice (fig. S1C).

Resistance to HFD-induced obesity in *Hacd1*-KO mice could be explained either by a reduction in energy intake or by an increase in energy substrate expenditure. Analysis of food consumption revealed similar energy intake per animal for both genotypes (fig. S1D) and, thus, higher energy intake per gram of body mass in *Hacd1*-KO mice, considering their lower mass (fig. S1E). Fecal lipid content was similar between genotypes (fig. S1F), excluding defective intestinal absorption as a cause of energy loss. Together, feed efficiency, i.e., body weight gain per eaten calories, was markedly reduced in *Hacd1*-KO mice (Fig. 1H), pointing to increased energy substrate expenditure as causative for the observed resistance to HFD-induced obesity.

An indirect calorimetry analysis of metabolic efficiency was performed both in normal diet (ND) and after a switch to HFD. After acclimatization to HFD, energy expenditure was higher at every time point in *Hacd1*-KO mice than in WT mice, resulting in a significant increase in energy expenditure over a 24-hour period (Fig. 1I). Basal metabolism was found significantly increased in *Hacd1*-KO mice compared to WT, both during day and night periods (Fig. 1J).

Increased energy expenditure and reduced feed efficiency were also found in ND, but to a lesser extent than in HFD (fig. S1, G and H), indicating that resistance to HFD-induced obesity of *Hacd1*-KO mice was linked to a preexisting metabolic feature that diverted energy from storage and was magnified upon exposure to lipid-based substrate.

Brown adipose tissue (BAT) has a specific capacity to dissipate energy through heat production by mitochondrial uncoupling due to proton leakage by uncoupling proteins (UCP) through the IMM (*8*). BAT mass was found to be reduced in *Hacd1*-KO mice compared to WT (table S1), and expression of *Ucp* genes was similar between genotypes in BAT and in other metabolically active tissues (fig. S1, I to K), thus excluding BAT involvement in the higher energy expenditure of *Hacd1*-KO mice. Since muscle mass represents a substantial pole of energy expenditure, we next explored the contribution of skeletal muscle in the metabolic phenotype observed in *Hacd1*-KO mice.

Oxidative capacities are increased in the skeletal muscles of *Hacd1*-KO mice

Expression of *Hacd1-fl* mRNA that encodes the catalytically active isoform of *Hacd1* is nearly restricted to striated muscles (*20*); hence, we decided to investigate heart and skeletal muscle function in *Hacd1*-KO mice. In-depth echocardiographic analysis of heart function revealed no difference between WT and *Hacd1*-KO mice (table S2). On the contrary, we observed a metabolic switch of skeletal muscle fibers toward a more oxidative, less glycolytic activity in *Hacd1*-KO mice. First observed on histological sections of the mixed tibialis anterior muscle (Fig. 2A), the oxidative switch was exemplified by a higher mitochondrial cytochrome *c* oxidase (COX) activity both in soleus and superficial gastrocnemius muscles, which are oxidative and glycolytic, respectively (Fig. 2B). Quantification of citrate synthase (CS) activity and protein content along with CV-ATP5A and VDAC mitochondrial proteins expression confirmed an increase in mitochondrial mass in *Hacd1*-KO skeletal muscle (Fig. 2, C to E), which was linked to increased expression of mitochondrial biogenesis promoters such as the *Ppargc1a (PGC-1alpha)*, *Ppargc1b (PGC-1beta)*, *Tfam*, and *Nrf-1* genes (fig. S2A). Noteworthy, mitochondrial mass was unchanged in heart, liver, WAT, and BAT (fig. S2, B and C).

The higher oxidative activity was associated with elevated fat oxidation by *Hacd1*-KO mice during the night, a period normally characterized by low-fat oxidation (Fig. 2, F and G). Accordingly, skeletal muscle showed increased capacity to oxidize fatty acids in vitro (Fig. 2H). This metabolic switch was accompanied by transcriptional changes in muscle characterized by an up-regulation of genes involved in fatty acid β-oxidation and lipid signaling pathways and a reciprocal decrease in lipogenesis genes (fig. S2D). This transcriptional signature was not observed in other metabolically active tissues such as the heart, liver, WAT, and BAT (fig. S2E). Furthermore, a nontargeted large-scale proteomic analysis (*24*) revealed that 37% of the up-regulated proteins were involved in metabolic processes (fig. S2F and table S3), in particular, the mitochondrial tricarboxylic acid cycle pathway was overrepresented by a factor of 37.5 ($P = 0.0143$) (fig. S2G and table S3). Together, these results point to a specific elevation of mitochondrial oxidative activity in

Downloaded from http://advances.sciencemag.org/ on January 26, 2021

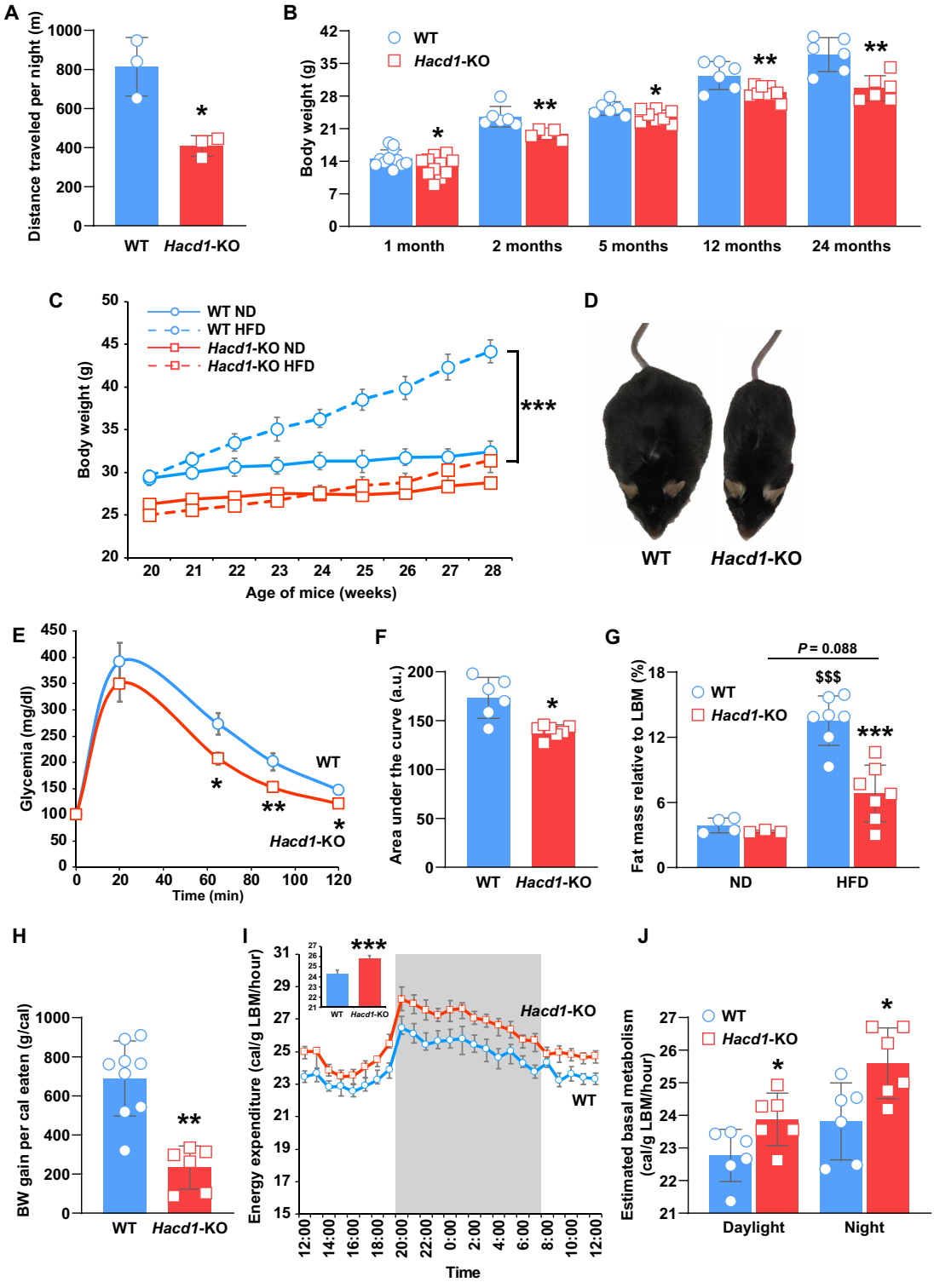


Fig. 1. Increased energy expenditure protects *Hacd1*-KO mice against HFD-induced obesity. (**A**) Spontaneous distance traveled per night by wild-type (WT) and *Hacd1*-KO mice. (**B**) Body weight evolution over life. (**C**) Body weight evolution of mice fed during 9 weeks with HFD, compared to age-matched mice fed with normal diet (ND). (**D**) Morphology of WT and *Hacd1*-KO mice after 9 weeks of HFD. (**E**) Glycemia measured after fasting and assessed during 120 min after an intraperitoneal glucose injection at T_0 in mice fed during 9 weeks with HFD. (**F**) Area under the glycemia curves displayed in (E). a.u., arbitrary units. (**G**) Total body fat percentage (adiposity index) after 9 weeks of ND or HFD, expressed as a percentage of the eviscerated body mass (lean body mass, LBM). (**H**) Feed efficiency during the 9-week period of HFD (body weight, BW). (**I**) Circadian energy expenditure measured by indirect calorimetry under HFD; the active period of night is shaded. Mean hourly energy expenditure during the assessment period is represented as histogram. (**J**) Estimated basal metabolism during the assessment period of (I) during daylight and night. Error bars ± SE; $^{*}P < 0.05$, $^{**}P < 0.01$, and $^{***}P < 0.001$ versus respective WT values; $^{\$\$\$}P < 0.001$ versus respective ND values. Photo credit for (D): Alexandre Prola, EnvA.

Downloaded from http://advances.sciencemag.org/ on January 26, 2021

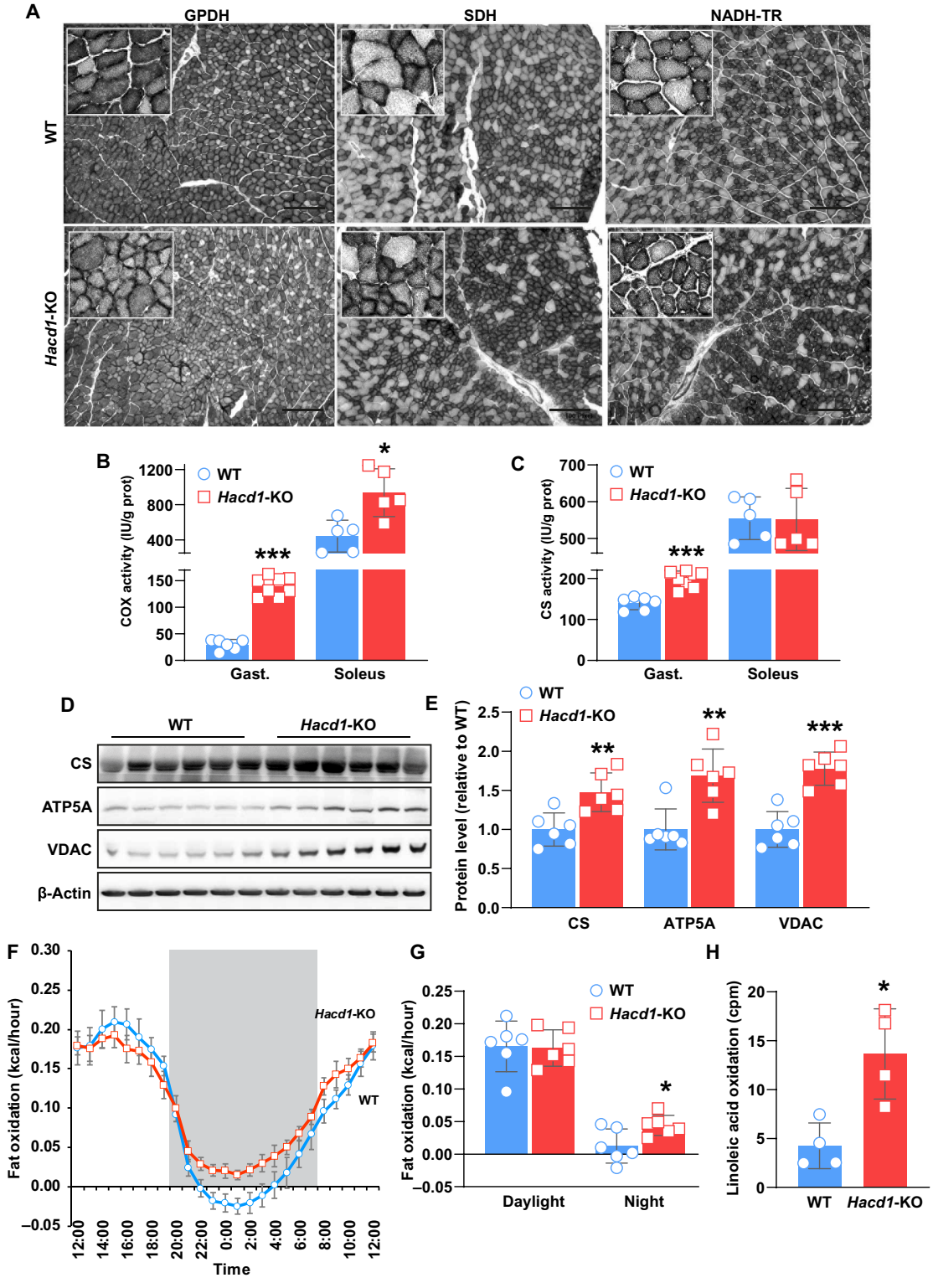


Fig. 2. Skeletal muscle of *Hacd1*-KO mice displays increased oxidative activity. (**A**) Glycerol-3-phosphate dehydrogenase (GPDH), succinate dehydrogenase (SDH), and reduced form of nicotinamide adenine dinucleotide (NADH) dehydrogenase (NADH tetrazolium reductase reaction, NADH-TR) activity on tibialis anterior muscle sections. Note the decreased GPDH (glycolytic) and increased SDH and NADH-TR (oxidative) activity on *Hacd1*-KO mice sections. (**B**) Cytochrome *c* oxidase (COX; or complex IV) activity in superficial gastrocnemius and soleus muscles. (**C**) CS activity in superficial gastrocnemius and soleus muscles. IU, International Unit. (**D** and **E**) Representative immunoblots (D) and quantification (E) of CS, ATP5A, and VDAC normalized to β-actin in superficial gastrocnemius muscle. (**F**) Circadian fat oxidation under ND measured by indirect calorimetry; the active period of night is shaded. (**G**) Fat oxidation during the assessment period of (**F**) during daylight and night. (**H**) ^{14}C-labeled linoleic acid consumption rates in isolated gastrocnemius muscle. Scale bars, 200 μm (A). Error bars ± SE; **P* < 0.05, ***P* < 0.01, and ****P* < 0.001 versus respective WT values.

Downloaded from http://advances.sciencemag.org/ on January 26, 2021

skeletal muscles as a driving force for the lipid-based substrate preference and elevated energy expenditure observed in *Hacd1*-KO mice.

HACD1 deficiency is associated with increased energy dissipation in skeletal muscle mitochondria

Because *Hacd1*-KO mice had reduced locomotor activity, we excluded the hypothesis that the increased oxidative activity sustained enhanced muscle contractility. We thus investigated whether it would reflect a reduced mitochondrial efficiency in ATP production in skeletal muscle, which would drive more energy substrate consumption.

Ultrastructural analysis of mitochondria by electron microscopy in both soleus and gastrocnemius muscles revealed a high proportion of altered cristae, with global enlargement and frequent tip dilation (Fig. 3, A to C, and fig. S3, A to C). Furthermore, evaluation of respiratory parameters was performed on isolated mitochondria from tibialis anterior muscle (Fig. 3, D and E, and table S4). Whereas basal, nonphosphorylating oxidation was similar in *Hacd1*-KO and WT mice, phosphorylating oxidation that links proton transfer to ATP production was markedly reduced (Fig. 3D), leading to a strong decrease in the respiratory coupling ratio, i.e., the ratio between coupled and uncoupled phosphorylation (Fig. 3E). Accordingly, the ATP production flux by muscle mitochondria was reduced (Fig. 3F), leading to a diminished ATP/O ratio indicative of deficient mitochondrial OXPHOS yield (Fig. 3G). When considering the increased mitochondrial mass of muscle fibers in *Hacd1*-KO mice (Fig. 2, B to E), consistent results were obtained on permeabilized muscle fibers from soleus and gastrocnemius muscles, both with pyruvate and fatty acid as a substrate (fig. S3, D to I, and table S4), confirming that reduced mitochondrial coupling was a general feature of skeletal muscles in *Hacd1*-KO mice. Noteworthy, permeabilized cardiac fibers showed normal respiratory parameters (fig. S3, J to L), restricting the mitochondrial perturbation to skeletal muscles.

To further evaluate consequences of a reduced skeletal muscle mitochondrial efficiency in vivo, we challenged mice with a submaximal treadmill exercise. In *Hacd1*-KO mice compared to WT, we quantified a significant twofold reduction in skeletal muscle ATP content after the exercise (Fig. 3H). Accordingly, phosphorylation of the adenosine 5′-monophosphate–activated protein kinase (AMPK) energy sensor was increased in muscle after exercise in *Hacd1*-KO mice, as well as blood lactate concentration (Fig. 3, I to K).

A muscle mitochondrial reduced coupling distinct from the canonical uncoupling

Hacd1-related mitochondrial perturbation in skeletal muscle was accompanied by neither detectable modification of redox potential in both states 3 and 4 (fig. S4A), nor difference in the generation of $\Delta\Psi m$ in state 4 (fig. S4B). This demonstrated that successive steps of reduced form of nicotinamide adenine dinucleotide (NADH) production by dehydrogenases, NADH consumption by the respiratory chain, and establishment of proton gradient by the respiratory chain, respectively, were all unaffected. Contrasting with conditions harboring specific ATP synthase deficiency (*25*), consumption of $\Delta\Psi m$ in state 3 was also normal (fig. S4B). Besides, preserved nonphosphorylating respiration indicated that proton leak was unchanged (Fig. 3D). These data confirmed that the reduced mitochondrial coupling characterized in skeletal muscles of *Hacd1*-KO mice is distinct from the canonical uncoupling. It induced no oxidative stress, as evidenced by normal ratio of aconitase/fumarase activities, expression of antioxidant genes and content of peroxidated lipids or carbonylated proteins (fig. S4, C to G). Also, the assembly of the supercomplexes, the oligomerization of ATP synthase, and the mitochondrial translocase activity, providing ADP to the ATP synthase, were all normal (fig. S4, H to J). Together, these results excluded an intrinsic defective function of the respiratory chain or the ATP synthase in *Hacd1*-deficient muscles, and rather suggested a functional impairment of proton transfer from the respiratory chain to the ATP synthase.

Mitochondrial coupling efficiency in skeletal muscle depends on cardiolipin content

Given the role of *Hacd1* in the VLCFA elongation cycle, we wondered how its deficiency would alter the composition or content of the key lipids within the IMM that may be involved in the supply of protons to ATP synthase. Cardiolipin is a phospholipid specifically enriched in the IMM that has been involved in proper cristae folding (*12*, *13*). Furthermore, its negative charge and abundance argue for specific interactions with protons (*26*).

Quantification of cardiolipin in skeletal muscle mitochondria from *Hacd1*-KO mice showed a significant decrease in both its absolute and relative content (Fig. 4A and fig. S5, A and B), whereas it was unchanged in cardiac mitochondria (fig. S5, C and D). Cardiolipin contains four variable acyl chains and forms a family of distinct species whose repartition is tightly controlled in cardiac and skeletal muscles (*27*). The slight reduction in the C18-C26/C10-C17 fatty acids ratio observed in mitochondria of *Hacd1*-KO mice had no impact on cardiolipin repartition (fig. S5, E and F). The comprehensive quantification of cardiolipin species in skeletal muscles of *Hacd1*-KO mice revealed an unchanged overall repartition (Fig. 4B and fig. S6, A to D). To document the consequences of the reduction in cardiolipin content beyond the observed abnormalities of cristae, we analyzed the properties of the IMM, and we quantified changes in the longest lifetime components in 1-(4-trimethylammoniophenyl)-6-phenyl-1,3,5-hexatriene *p*-toluenesulfonate (TMA-DPH) fluorescence lifetime decay that reflect the behavior of the probe within the most polar membrane domains (fig. S6E, table S5, and listing S1) (*28*).

Furthermore, to investigate whether the reduced cardiolipin content could be a limiting factor for ATP production in the specific context of HACD1 deficiency, we set up an original in vitro assay to enrich mitochondrial membranes with cardiolipin or phosphatidylcholine, a neutral and abundant phospholipid slightly increased in *Hacd1*-deficient muscle mitochondria (Fig. 4C and fig. S5B). Incorporation of the two phospholipids within the IMM was validated using fluorescent species (fig. S6F). The proof for cardiolipin enrichment in mitochondria, and more specifically in mitoplasts, was further obtained by the increased Acridine Orange 10-Nonyl Bromide (NAO probe) signal (fig. S6, G and H). Using this system, we then simultaneously measured O_2 consumption and ATP production of mitochondria and found a nonspecific decreased O_2 consumption and lowered ATP production after cardiolipin or phosphatidylcholine enrichment, under both *Hacd1*-KO and WT conditions (fig. S6, I and J). This may be due to respiratory chain complexes dilution within the membrane (*29*) or to an impairment in lipid arrangement following phospholipid enrichment. Noteworthy, specific enrichment of mitochondria from *Hacd1*-KO mice with cardiolipin fully rescued the ATP/O ratio that reflects coupling efficiency of ATP synthase activity with the respiratory chain function, while the ratio was markedly decreased by phosphatidylcholine enrichment under both *Hacd1*-KO and WT conditions (Fig. 4D). Together, these data

Downloaded from http://advances.sciencemag.org/ on January 26, 2021

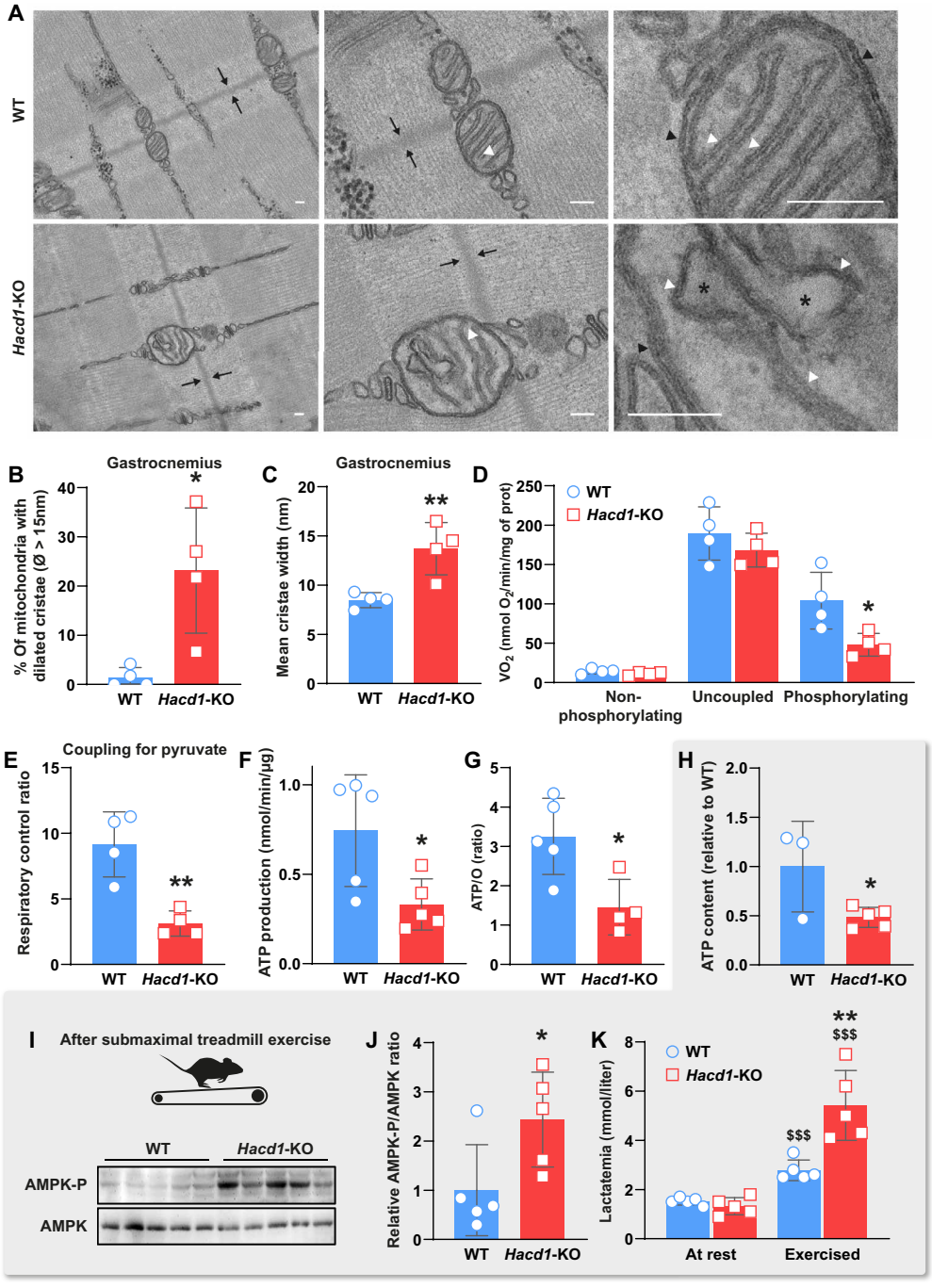


Fig. 3. Remodeled structure and lowered respiratory coupling of mitochondria lead to reduced ATP production in muscle of *Hacd1*-KO mice. (**A**) Transmission electron microscopy of longitudinal sections of myofibers from the superficial gastrocnemius muscle. Images are from datasets taken at a low (×2500, left), intermediate (×10,000, middle), and high (×30,000, right) magnification. The *Z* line is delimited by arrows. Cristae are regular tubular-shaped invaginations (white arrow heads) of the IMM, unambiguously identified on the same plane than the outer mitochondrial membrane (black arrow heads). Excessive dilation of cristae tips (asterisk) is frequently observed in *Hacd1*-KO myofibers. (**B** and **C**) Morphometric quantification of mitochondria containing cristae with excessively dilated tips (maximal diameter > 15 nm, in percentage) (B) and the mean of the maximal diameter of cristae (C). (**D**) Oxidation rate of freshly isolated mitochondria from tibialis anterior muscle in the presence of pyruvate plus ADP (phosphorylating), oligomycin (nonphosphorylating), and FCCP (uncoupled). (**E**) Mitochondrial coupling ratio for pyruvate (respiratory control ratio [RCR; state 3/state 4)] of isolated mitochondria from tibialis anterior muscle. (**F**) ATP production measured on isolated mitochondria from tibialis anterior muscle. (**G**) ATP/O ratio calculated from simultaneous recording of O_2 consumption and ATP production on isolated mitochondria from tibialis anterior muscle. (**H**) ATP content after submaximal exercise on treadmill in tibialis anterior muscle of *Hacd1*-KO mice, compared to WT mice, set to 1.0. (**I** to **J**) Representative immunoblots (I) and quantification (J) of phospho-AMPK (adenosine 5′-monophosphate–activated protein kinase) and AMPK in tibialis anterior muscle after submaximal exercise on treadmill. (**K**) Blood lactate concentration (lactatemia) before (at rest) and after (exercised) a submaximal exercise on treadmill. Scale bars, 100 nm (A). Error bars ± SE; $^{*}P < 0.05$ and $^{**}P < 0.01$ versus respective WT values; $^{\$\$\$}P < 0.001$ versus respective at rest values.

Downloaded from http://advances.sciencemag.org/ on January 26, 2021

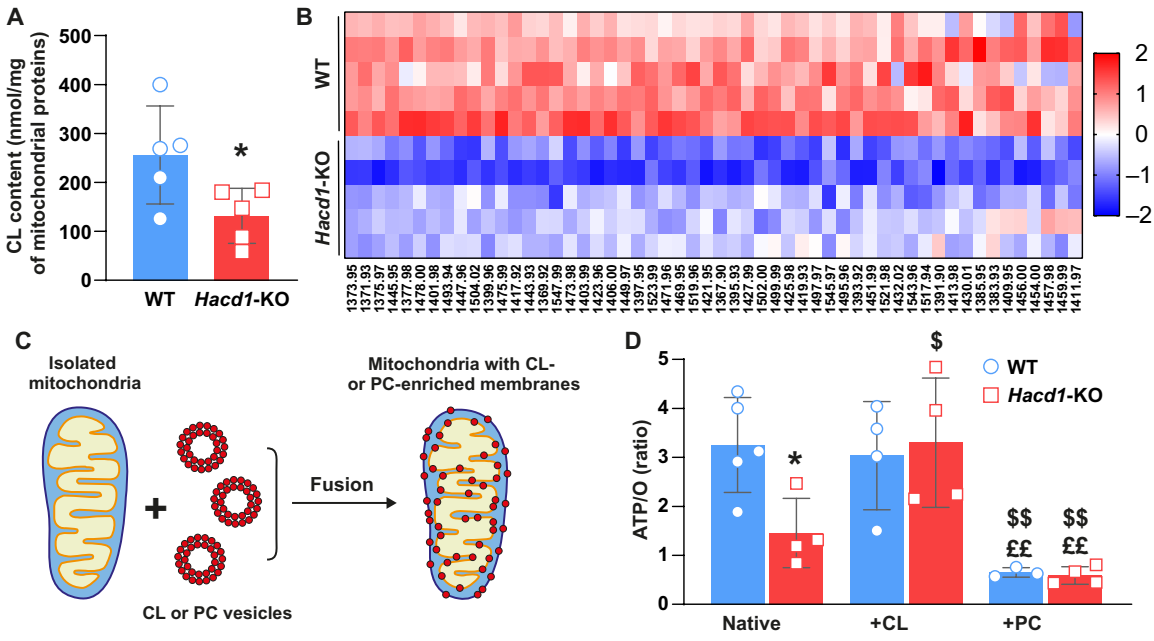


Fig. 4. Cardiolipin deficit in muscle mitochondria of *Hacd1*-KO mice is responsible for reduced mitochondrial coupling. (**A**) Total cardiolipin content of mitochondria isolated from the tibialis anterior muscle, normalized to the mitochondrial protein content. (**B**) Heatmap of individually identified cardiolipin species in mitochondria isolated from tibialis anterior muscle of *Hacd1*-KO mice, compared to WT mice. Colors show row *z* scores. (**C**) Diagram depicting the experimental steps allowing to enrich mitochondrial membranes with phospholipids. (**D**) ATP/O ratio calculated from simultaneous recording of O_2 consumption and ATP production of native, cardiolipin-enriched (+CL), and phosphatidylcholine-enriched (+PC) mitochondria isolated from tibialis anterior muscle of WT and *Hacd1*-KO mice. Error bars ± SEM.; $^*P < 0.05$ versus WT, $^{\$}P \leq 0.05$ and $^{\$\$}P \leq 0.01$ versus native, and $^{££}P \leq 0.01$ versus +CL.

demonstrate that efficient mitochondrial coupling in skeletal muscle depends on the cardiolipin content that is genetically controlled by *Hacd1* expression.

DISCUSSION

In this study, we describe that lack of *Hacd1*/VLCFA-dependent synthesis of the IMM phospholipid cardiolipin in skeletal muscles leads to whole-body protection against HFD-induced obesity through an atypical mechanism of reduced mitochondrial coupling efficiency that drives a shift toward increased lipid oxidation and basal energy expenditure.

We have identified that in *Hacd1*-KO mice, skeletal muscle is a site of increased energy consumption, fostered by a surge in oxidative activity as a compensating means to overcome an ATP production deficit, resulting from the reduced coupling efficiency of remodeled mitochondria. Molecularly, the reduced coupling between phosphorylating and nonphosphorylating respiration was associated with reduced cardiolipin content, and we demonstrated that the addition of cardiolipin to isolated mitochondria from *Hacd1*-KO mice rescued their coupling efficiency. This rescue experiment reveals a prominent role of cardiolipin content for a fully efficient mitochondrial coupling in skeletal muscle, which does not exclude a minor contribution, yet to be evaluated, of other phospholipids such as phosphatidylinositol.

Pharmacological induction of mitochondrial uncoupling with the aim of increasing lipid oxidation has been an appealing strategy to combat obesity and restore insulin sensitivity (*8*). Dinitrophenol (DNP), a potent mitochondrial uncoupling compound, was successfully used during three decades for weight loss, before being withdrawn in 1938 because of its toxicity, mostly in highly ATP-demanding tissues including the heart (*30*). Among recent promising strategies is a controlled-release formulation for DNP that specifically targets the liver (*31*). Here, we provide a genetic proof of concept that targeting the skeletal muscle and halving the mitochondrial coupling efficiency in this tissue induce protection against diet-induced obesity in mice, with improved insulin sensitivity, no oxidative stress, and a fully preserved cardiac function. These benefits occurred in mice that display a reduced skeletal muscle mass and locomotor activity, a situation mimicking the deleterious clinical condition of most obese patients (*6*, *7*). Our data represent in vivo demonstration that targeting a reduced coupling in skeletal muscle mitochondria is an actionable mechanism to confer protection against obesity, even in a context of low muscle mass and limited exercise capacity.

In parallel, our study provides evidence that the highly ATP-demanding skeletal muscle benefits from a specific genetic program for optimal mitochondrial efficiency and ATP production through *Hacd1* expression. HACD enzymes participate in the VLCFA elongation cycle, which has been implicated in specific lipid synthesis in skin, retina, brain, or testis (*18*). Our study extends the field of VLCFA elongation cycle to cardiolipin metabolism in skeletal muscle as cardiolipin content was reduced in this tissue in *Hacd1*-KO mice. Synthesis of cardiolipin, a four acyl-chain phospholipid specific of the IMM, is a complex process, with the last step consisting in remodeling of cardiolipin acyl chains by tafazzin, which results in an enrichment of linoleoyl chains (C18:2, ω-6) in heart and skeletal muscles (*27*). The functional importance of this reaction is illustrated by deleterious consequences of tafazzin deficiency, which induces the Barth syndrome characterized by a life-threatening infantile dilated

Downloaded from http://advances.sciencemag.org/ on January 26, 2021

cardiomyopathy (*15*, *16*). Notably, acyl chain repartition among cardiolipin species was unchanged in HACD1-deficient muscle mitochondria, indicating that the tafazzin-dependent step of cardiolipin maturation was unaffected. *Hacd1* is also expressed in the heart (*20*) but, serendipitously, its deficiency had no impact on cardiac mitochondrial function, likely because the redundant paralogous *Hacd* genes, highly expressed in the heart [our observations, (*19*, *32*)], perform HACD activity in this tissue.

Our study identified a specific context of mitochondrial perturbation that suggests a direct role for cardiolipin in mitochondrial coupling efficiency. We measured normal V_0 (i.e., O_2 consumption without ADP), which ruled out canonical uncoupling via increased proton leakage through the IMM. Furthermore, careful analysis of respiratory parameters observed in *Hacd1*-KO mice revealed normal activity of the respiratory chain (i.e., of complexes I to IV) and analysis of ATP synthase oligomerization and ADP kinetics identified no change in *Hacd1*-KO mice compared to WT. The molecular mechanism that leads to a decreased phosphorylation capacity in mitochondria of HACD1-deficient muscles is therefore based neither on the classical uncoupling mechanism nor on the defective functioning of the respiratory chain or ATP synthase. Cardiolipin has been proposed to favor strong cristae curvatures, assembly of tightly packed lipid-protein complexes (*33*, *34*), and mitochondrial respiratory efficiency (*11*, *12*, *14*, *35*). Contrarily to models completely lacking cardiolipin (*33*, *34*), our model of *Hacd1* deficiency, with a halving of the cardiolipin content, preserved assembly of respiratory supercomplexes and ATP synthase oligomerization. However, the reduction in cardiolipin content was associated with a reduction in mitochondrial coupling efficiency, and our in vitro demonstration that the addition of cardiolipin rescued mitochondrial coupling of mitochondria isolated from *Hacd1*-deficient muscle confirms a direct role of cardiolipin in the ATP production efficiency (*14*, *35*). Further exploration of respiratory parameters in this context would be instrumental in unraveling the molecular mechanisms underlying the contribution of cardiolipin to mitochondrial coupling. Among these is a possible role in facilitating the lateral transfer of protons from respiratory complexes to ATP synthase (*36*–*40*), enabled by the abundance and negative charge of cardiolipin (*26*). In parallel, several studies report transient binding of cardiolipin to ATP synthase that contributes to its efficiency, possibly through lubrification of the ATP synthase ring or facilitated proton translocation (*14*, *41*). All of these data are consistent with previous observations postulating a local proton circuitry at the microdomain level within the IMM for the benefit of optimized ATP synthase efficiency (*39*, *42*–*44*).

Overall, our data identify that the cardiolipin content of skeletal muscle governs the energy balance of the body and open up new insights into understanding the molecular mechanisms for efficient OXPHOS in the mitochondria. While future studies are warranted to support the potential of translation of this phenomenon, the mechanism that we have discovered is promising for the development of new strategies for the prevention or treatment of metabolic disorders.

MATERIALS AND METHODS

Mice

Experiments on mice were approved by the Anses/EnvA/Upec Ethics Committee (C2EA-16; approval numbers 11/11/15-2, 20/12/12-16, and 17-030), and all care and manipulations were performed in accordance with national and European legislation on animal experimentation. The whole study was carried on male mice that were housed in stainless steel cages containing environmental enrichment, in rooms maintained at 22° ± 1°C with an air change rate of 12 vol/hour and lit from 7 a.m. to 7 p.m. Food and water were given ad libitum unless otherwise stated. *Hacd1*-KO mice were generated as previously described (*20*). Food was either an ND [3188 kcal/kg from carbohydrates (64%), proteins (24%), and fat (12%); maintenance diet for mice #C1324, Altromin] or an HFD [5241 kcal/kg from fat (60%), carbohydrates (23%), and protein (17%); diet-induced obesity diet #C1090, Altromin]. Kcal% was related to metabolizable energy (calculated values). Mice assessed for body mass gain under ND or HFD were housed individually, and mice body mass and food intake were measured each week. Food efficiency was determined by dividing the body mass gain (mg) by the total calorie intake (kcal). Mice were euthanized by cervical dislocation. The fast-twitch glycolytic superficial gastrocnemius, fast-twitch oxidative glycolytic (mixed) tibialis anterior, and the slow-twitch soleus muscle were used to provide a representative panel of muscles with different myofiber composition. In the whole study, BAT refers to interscapular BAT.

Spontaneous locomotor activity

Spontaneous locomotor activity was measured over a 12-hour night period using the Activmeter system (Bioseb). During the experiment, mice (4 to 5 months old) were individually caged with food and water provided ad libitum. The system allowed to quantify movements of the animal (distance, duration, slow versus fast movements, and average speed of the animal when it is in motion) and the time and duration of immobility. After a 24-hour period of acclimation, locomotor activity was recorded during four consecutive nights.

Treadmill test

The running capacity was evaluated on a treadmill (Tecmachine, Medical Development) at a 4% slope. All mice (4 to 5 months old) were initially acclimatized to the treadmill for 5 days (10 min/day and 12 m/min). The maximal aerobic speed was determined by challenging mice to an exercise of progressively increased intensity. Speed was increased every 2 min and the speed of the last completed running step before exhaustion was considered as the individual maximal aerobic speed. Endurance capacity was determined by challenging mice to a submaximal exercise intensity (60% of the maximal aerobic speed) until exhaustion.

Blood lactate concentration

A droplet of capillary blood was produced through incision of the tip of the tail. The tail and the droplet were brought close to the tip of the sensor so that the blood was absorbed and reached the measurement chamber of a LactateScout+ device (EKF Diagnostics, Germany).

Glucose tolerance test

The glucose tolerance test was performed in mice (7 months old) fasted overnight for 16 hours before an intraperitoneal injection of a 40% glucose in normal saline solution at a dose of 3 g of glucose per kilogram of body mass for ND-fed mice or glucose (1 g/kg) for HFD-fed mice. Blood was sampled from the tail vein just before the injection (T_0) and then after 30, 60, 90, and 120 min to assay blood glucose concentration (glycemia; Contour XT glucometer; Bayer).

Downloaded from http://advances.sciencemag.org/ on January 26, 2021

Indirect calorimetry study

Mice (4 months old) were individually housed 14 days before and presented with training bottle and acclimated to the chambers for 48 hours before experimental measurements. For the experiment, they were fed 7 days with ND and then 7 days with HFD. They were analyzed for whole energy expenditure, oxygen consumption and carbon dioxide production, RQ (VCO_2/VO_2), food intake, and locomotor activity (beam breaks per hour) using a calorimetric device (LabMaster, TSE Systems GmbH). Data were recorded every 15 min for each animal during the entire experiment. Data analysis was performed on excel XP using extracted raw value of VO_2 consumed, VCO_2 production (expressed in milliliter per hour), and energy expenditure (kilocalories per hour). Subsequently, each value was normalized to the whole lean body mass extracted from the EchoMRI (Whole Body Composition Analyzers, EchoMRI, Houston, TX, USA) analysis as previously described (*45*). No practical method of estimation of the basal metabolism is available presently. However, an estimation could be made from windows of time during which animals should have no access to food, their previous intake had been far enough in time to discard the thermic effect of food, and the spontaneous activity had been the lowest possible within the past 30 min. Data points of energy expenditure were considered as the best estimation of basal metabolism when the spontaneous activity was lower, within the last 30 min, than 5% of the highest daily value and when no intake was recorded within the last 60 min. Fatty acid oxidation was calculated from the following equation: fat ox (kcal/hour) = energy expenditure (kcal/hour) × (1-RER/0,3) according to (*46*).

Echocardiography

Mice (7 months old) were trained to be grasped because transthoracic echocardiography was performed in nonsedated mice to avoid any cardiac depressor effect of anesthetic agents. Typical heart rates at recording were above 600 beats per minute (bpm). Mice were carefully caught by the left hand and placed in supine position. Images were acquired from a parasternal position at the level of the papillary muscles using a 13-MHz linear-array transducer with a digital ultrasound system (Vivid 7, GE Medical System, Horton, Norway). Left ventricular (LV) diameters and anterior and posterior wall thicknesses were serially obtained from M-mode acquisition. As we expected a homogenous function and planned to compare sequential echocardiography, we used M-mode technique to assess both LV volumes, mass, and ejection fraction. Relative LV wall thickness was defined as the sum of septal and posterior wall thickness over LV end-diastolic diameter, and LV mass was determined using the uncorrected cube assumption formula [LV mass = (AWTdþ LVEDDþ PWTd)^3 – (LVEDD)^3]. Diastolic function was not assessed by echocardiography because of the heart rate above 600 bpm precluding the analysis of transmitral flow. Therefore, we assessed relaxation by dP/dt_{min} during in vivo hemodynamic analysis. Peak systolic values of radial Strain rate (SR) in the anterior and posterior wall were obtained using tissue Doppler imaging (TDI) as previously described (*47*). TDI loops were acquired from the same parasternal view with a careful alignment with the radial component of the deformation (*48*) at a mean frame rate of 514 frames per second and a depth of 1 cm. The Nyquist velocity limit was set at 12 cm/s. Radial SR analysis was performed offline using the EchoPac Software (GE Medical Systems) by a single observer (G.D.) blinded to the genotype of the animals. Peak systolic of radial SR was computed from a region of interest positioned in the mid-anterior wall and was measured over an axial distance of 0.6 mm. The temporal smoothing filters were turned off for all measurements. Because slight respiratory variations exist, we averaged peak systolic of radial SR on eight consecutive cardiac cycles. The intra-observer variability of radial SR was assessed (G.D.) using the same acquisition and same method at 24-hour intervals [3.5 ± 3.4% (3.3 to 3.7)].

Extraction of total RNA, RT-PCR, and RT-qPCR analyses

Samples from 4-month-old mice were snap-frozen in liquid nitrogen and stored at −80°C. Total RNAs were isolated using TRIzol reagent (Sigma-Aldrich) according to the manufacturer's protocol. Purity of RNAs was assessed by a ratio of absorbance at 260 and 230 nm > 1.7. RNA quality was checked on agarose gel. One microgram of RNA was used for reverse transcription with the Maxima First Strand complementary DNA (cDNA) Synthesis Kit for reverse transcription quantitative polymerase chain reaction (RT-qPCR) (Fermentas). cDNAs were amplified using the Maxima SYBR Green qPCR Master Mix (2×; Fermentas). qPCR reactions were performed on a Roche Light Cycler system (Roche). All PCR and qPCR products were examined qualitatively on agarose gels. All presented RT-qPCR results were normalized by the geometrical mean of three independent reference genes (*Ywhaz*, *Polr2a*, and *Rplpo*), as previously described (*49*). Sequences of primers are listed in table S6.

Western blot experiments

Frozen tissues from 4- to 7-month-old mice were lysed in RIPA lysis buffer [50 mM tris-HCl (pH 8), 150 mM NaCl, 1% Triton X-100, 1 mM EDTA, 0.1% SDS, and 0.5% deoxycholic acid], supplemented with a cocktail of protease and phosphatase inhibitors (Pierce), using a Precellys homogenizer (Bertin). Protein concentration was assessed using the bicinchoninic acid assay (Pierce). Protein extracts (20 µg) from superficial gastrocnemius muscles of 6-month-old WT and *Hacd1*-KO mice were loaded on Bolt 4 to 12% bis-tris gels (Invitrogen), separated for 22 min at 200 V and subsequently transferred to polyvinylidene difluoride membranes using transfer stack and iblot2 system for 7 min at 20 V (Invitrogen). Thereafter, blots were blocked for 60 min in 1.25% gelatin in tris-buffered saline with Tween 20 at room temperature, followed by incubation with different primary antibodies [phospho-AMPK, AMPK, and CS from Cell Signaling; ATP5A from Abcam; VDAC (custom-made gift from C. Lemaire, INSERM U1180)], overnight at 4°C. After washing, membranes were incubated with the appropriate secondary antibodies for 60 min at room temperature and revealed using the West Femto chemiluminescent substrate (Pierce). Light emission was recorded using a chemiluminescent detection system (G-Box, Syngene) and quantified by the ImageJ software [v1.47, National Institutes of Health (NIH)]. Protein content was normalized to β-actin (Antibody from Santa Cruz Biotechnology).

Proteomic analyses

Muscle lysates of tibialis anterior from 4-month-old mice were loaded on a gel, and each lane of gel was cut and washed for 15 min with an acetonitrile (ACN)/100 mM ammonium bicarbonate mixture (1:1). Digestion was performed in 50 mM ammonium bicarbonate (pH 8.0) and the quantity of modified trypsin (Promega, sequencing grade) was 0.1 µg per sample. Digestion was achieved for 6 hours at 37°C. The supernatant was conserved. Peptides were extracted by 5% formic acid in water/ACN (v/v). Supernatant and

Downloaded from http://advances.sciencemag.org/ on January 26, 2021

extract tryptic peptides were dried and resuspended in 20 µl of 0.1% (v/v) trifluoroacetic acid (TFA). High-performance liquid chromatography was performed on an Ultimate 3000 LC system (Dionex). A 4-µl sample was loaded at 20 µl/min on a precolumn cartridge [stationary phase: C18 PepMap 100, 5 µm; column: 300-µm inside diameter (i.d.), 5 mm; Dionex] and desalted with 0.08% TFA and 2% ACN. After 4 min, the precolumn cartridge was connected to the separating PepMap C18 column (stationary phase: C18 PepMap 100, 3 µm; column: 75-µm i.d., 150 mm; Dionex). Buffers were 0.1% HCOOH and 2% ACN (A) and 0.1% HCOOH and 80% ACN (B). The peptide separation was achieved with a linear gradient from 0 to 36% B for 18 min at 300 nl/min. Including the regeneration step at 100% B and the equilibration step at 100% A, one run took 50 min. Eluted peptides were analyzed online with a LTQ-Orbitrap mass spectrometer (MS; Thermo Electron) using a nanoelectrospray interface. Ionization (1.35-kV ionization potential) was performed with liquid junction and a capillary probe (10-µm i.d.; New Objective). Peptide ions were analyzed using Xcalibur 2.07 with the following data-dependent acquisition steps: (i) full MS scan in Orbitrap [mass-to-charge ratio (*m*/*z*) 300 to 1600, profile mode] and (ii) MS/MS in linear Trap (qz, 0.25; activation time, 30 ms; and collision energy, 35%; centroid mode). Step 2 was repeated for the four major ions detected in step 1. Dynamic exclusion time was set to 60 s. A database search was performed with XTandem (X! tandem CYCLONE version 2010.12.01.1, http://thegpm.org/TANDEM/). Enzymatic cleavage was declared as a trypsin digestion with one possible miss cleavage. Cys carboxyamidomethylation and Met oxidation were set to static and possible modifications, respectively. Precursor mass and fragment mass tolerance were 10 parts per million and 0.5 Da, respectively. A refinement search was added with similar parameters except that semi-trypsic peptide and possible N-terminal proteins acetylation were searched. Few databases were used: the *Mus musculus* database (49,728 entries, version March 2011 from Uniprot), contaminant database (trypsin, keratins...). Only peptides with an *E* value smaller than 0.1 were reported. Identified proteins were filtered and grouped using XTandem Pipeline (version 3.1.4) (http://pappso.inra.fr/bioinfo/xtandempipeline/) according to: (i) A minimum of two different peptides was required with an *E* value smaller than 0.05 and (ii) a protein *E* value (calculated as the product of unique peptide *E* values) smaller than 10^{-4}. To take redundancy into account, proteins with at least one peptide in common were grouped. This allowed grouping proteins of similar function. Within each group, proteins with at least one specific peptide relatively to other members of the group were reported as subgroups. Gene Ontology analysis and protein set enrichment statistical analyses were performed using the PANTHER (Protein ANnotation THrough Evolutionary Relationship) classification system [www.pantherdb.org; (*24*)].

ATP quantification

Muscle ATP content was quantified using the CLSII kit (Sigma-Aldrich). Mice (4 to 5 months old) were euthanized immediately after a submaximal treadmill exercise of 40 min at 19 m/min and 4% slope, and tibialis anterior muscle was removed and snap-frozen in liquid nitrogen. Frozen tissues were weighted, minced with scissors, and homogenized in the lysis buffer provided in the kit using a Dounce homogenizer. Homogenates were centrifuged at 15,000*g* for 10 min and supernatants diluted 50:50 in the dilution buffer provided by the kit. ATP quantitation was performed according to the manufacturer's instructions. For each sample, ATP concentration was normalized to the total protein content assessed with the bicinchoninic acid assay (Pierce).

Isolation of skeletal muscles mitochondria and respiration measurement

Tibialis anterior muscles were quickly collected after euthanasia of mice (8 months old) in ice-cold phosphate-buffered saline (PBS) (Thermo Fisher Scientific) supplemented with 10 mM EDTA; muscle samples were then minced with scissors, rinsed, and incubated in 5 ml of ice-cold PBS supplemented with 10 mM EDTA and 0.05% trypsin for 30 min, followed by a centrifugation at 200*g* for 5 min. Pellets were suspended in isolation buffer 1 [67 mM sucrose, 50 mM KCl, 10 mM EDTA, 0.2% bovine serum albumin (BSA), and 50 mM tris-HCl (pH 7.4)] and homogenized with a Dounce homogenizer (Sigma-Aldrich). Mitochondria were purified by a differential centrifugation at 700*g* for 10 min, and mitochondria-containing supernatants were then centrifuged at 8000*g* for 10 min. The crude mitochondrial pellet was resuspended in an appropriate volume of isolation buffer 2 [250 mM sucrose, 3 mM EGTA, and 10 mM tris-HCl (pH 7.4)]. Protein concentration was assessed using the bicinchoninic acid assay (Pierce). The mitochondrial oxygen consumption flux was measured as previously described (*50*) at 37°C using 500 µg of crude mitochondria proteins diluted in 3 ml of mitochondrial respiration buffer [250 mM sucrose, 20 µM EGTA, 2 mM KH_2PO_4, 1 mM $MgCl_2$, and 10 mM tris-HCl (pH 7.4)] in an oxygraphic cell (Strathkelvin Instruments). The oxygen consumption rate was measured using 4 mM malate plus either 1 mM pyruvate and/or 1 mM pyruvate and 15 mM succinate. Oxygen consumption was assessed in the phosphorylating state with 4 mM ADP or in the nonphosphorylating state by adding oligomycin (2.5 µg/ml). Respiration was uncoupled by successive addition of carbonyl cyanide-4-(trifluoromethoxy) phenylhydrazone (FCCP) up to 5 µM to reach maximal respiration.

Measurement of ATP synthesis flux

Isolated mitochondria (65 µg/ml) from 4-month-old mice were resuspended in the mitochondrial respiration buffer (see above). After addition of ADP (4 mM), pyruvate (10 mM), glutamate (5 mM), and malate (5 mM), the oxygen consumption and ATP synthesis rates were both measured. Aliquots were collected every 60 s and precipitated in 7% $HClO_4$/25 mM EDTA, centrifuged at 16,000*g* for 5 min and then neutralized with 2 M KOH and 0.3 M MOPS. The ATP content in these samples was determined using the CLSII kit (Sigma-Aldrich). In a parallel experiment, oligomycin (2.5 µg/ml) was added to the mitochondrial suspension to determine the nonoxidative ATP synthesis rate.

Membrane potential measurement

The transmembrane potential variations ($\Delta\Psi$) were estimated in isolated mitochondria from 4-month-old mice from the fluorescence quenching of the lipophilic cationic dye rhodamine 123 using a Hitachi F7000 fluorimeter. Isolated mitochondria (65 µg of protein/ml) were incubated in the mitochondrial buffer [250 mM sucrose, 20 µM EGTA, 2 mM KH_2PO_4, 1 mM $MgCl_2$, and 10 mM tris-HCl (pH 7.4)] containing pyruvate (10 mM), glutamate (5 mM), malate (5 mM), and 0.66 µM of rhodamine 123 (Sigma-Aldrich), and thermostated at 37°C. When added, ADP was 1 mM and oligomycin was 2.5 µg/ml. The rhodamine 123 fluorescence signal at each steady state (*F*) was recorded using an excitation wavelength of 485 nm,

Downloaded from http://advances.sciencemag.org/ on January 26, 2021

and fluorescence emission was continuously detected at 500 nm. At the end of each experiment, the maximum fluorescence signal (F_{max}) was monitored after complete de-energization of the mitochondria following addition of FCCP (6 μM). Then, the $F_{max} - F/F_{max}$ difference at each steady state was calculated.

NAD (P)H/NAD (P)$^+$ redox measurement

Isolated mitochondria (100 μg of protein/ml) from 4-month-old mice were incubated in the mitochondrial buffer [250 mM sucrose, 20 μM EGTA, 2 mM KH_2PO_4, 1 mM $MgCl_2$, and 10 mM tris-HCl (pH 7.4)] thermostated at 37°C. When added, pyruvate was 10 mM, glutamate 5 mM, malate 5 mM, ADP 4 mM, and cyanide 4 mM. The NAD (P)H autofluorescence signal at each steady state (F) was recorded using an excitation wavelength of 340 nm, and fluorescence emission was continuously detected at 450 nm. At the end of each experiment, the maximum fluorescence signal (F_{max}) was monitored after complete reduction within the NAD (P)H/NAD (P)$^+$ couple following addition of cyanide. The fluorescence signal recorded in the presence of mitochondria alone without respiratory substrate was used as the 0% reduction state for the NAD (P)H/NAD (P)$^+$ couple. NAD (P)H/NAD (P)$^+$ ratio was expressed as a percentage of reduction according to the following formula: % reduction = (F – F0%) / (F100% – F0%) × 100.

Mitochondrial isolation from heart

Mice (8 months old) were euthanized, and hearts were quickly collected in ice-cold PBS (Thermo Fisher Scientific) supplemented with 10 mM EDTA; heart samples were then transferred into isolation buffer [310 mM sucrose, 20 mM tris-HCl, and 1 mM EGTA (pH 7.2)], minced with scissors and homogenized with a Dounce homogenizer (Sigma-Aldrich). Mitochondria were purified by a differential centrifugation at 1200g for 10 min, and mitochondria-containing supernatants were then centrifuged at 12,000g for 10 min. The crude mitochondrial pellet was resuspended in an appropriate volume of isolation buffer. Protein concentration was assessed using the bicinchoninic acid assay (Pierce).

Permeabilized muscle fibers respiration

The mitochondrial respiration was studied in vitro in saponin-skinned fibers as previously described (*51*). Briefly, fibers from 4-month-old mice were separated under a binocular microscope in solution S (see below) on ice and then permeabilized in solution S containing saponin (50 μg/ml) for 30 min at 4°C. After being placed 10 min in solution R (see below) to wash out adenine nucleotides and creatine phosphate, skinned separated fibers were transferred in a 3-ml water-jacketed oxygraphic cell (Strathkelvin Instruments) equipped with a Clark electrode, as previously described (*51*), under continuous stirring. Solution S contained: 2.77 mM CaK_2EGTA, 7.23 mM K_2EGTA, 20 mM taurine, 0.5 mM dithiothreitol (DTT), 20 mM imidazole, 50 mM potassium-methane sulfonate, 5.7 mM Na_2ATP, 15 mM creatine phosphate (final solution: pH 7.1, 160 mM ionic strength, 100 nM free Ca^{2+}, and 1 mM free Mg^{2+}). Solution R contained 2.77 mM CaK_2EGTA, 7.23 mM K_2EGTA, 20 mM taurine, 0.5 mM DTT, 20 mM imidazole, 3 mM phosphate, 90 mM potassium-methane sulfonate, 10 mM sodium-methane sulfonate, and fatty acid–free BSA (2 mg/ml), [final solution: pH 7.1, 160 mM ionic strength, 100 nM free Ca^{2+}, and 1 mM free Mg^{2+}]. After the experiments, fibers were harvested and dried, and respiration rates were expressed as micromoles of O_2 per minute and per gram of dry mass.

Measurement of the maximal muscular oxidative capacities

After the determination of basal respiration rate measured at 22°C with R solution plus 1 mM pyruvate and 4 mM malate as mitochondrial substrates (V_0, nonphosphorylating rate), fibers were exposed to an increasing concentration of ADP to determine the apparent Michaelis-Menten constant (Km) for ADP and maximal mitochondrial respiration [at saturating concentration of ADP (2 mM) V_{max}, phosphorylating rate]. The ratio of V_{max}/V_0 represented the degree of coupling between oxidation and phosphorylation of ADP for pyruvate.

Measurement of the respiratory chain complexes

While V_{max} was being recorded, electron flow went through complexes I, III, and IV. Then, 4 min after this V_{max} measurement, complex II was stimulated with succinate (15 mM) (complexes I, II, III, and IV). Complex I was then blocked with amytal (2 mM). Under these conditions, mitochondrial respiration was evaluated by complexes II, III, and IV.

Measurement of mitochondrial substrate utilization

Experiments were started in solution R plus 4 mM malate, 2 mM carnitine, and 0.1 mM palmitoyl-CoA (PCoA). After the determination of basal respiration rate V_0, the maximal fiber respiration rate of PCoA was measured in the presence of a saturating ADP concentration (2 mM). Then, substrates were sequentially added every 3 to 4 min as follows: 0.1 mM octanoate, 1 mM pyruvate, and 15 mM succinate. The ratio PCoA/V_0 corresponded to the degree of coupling between oxidation and phosphorylation for this substrate.

Supramolecular organization of mitochondrial respiratory chain complexes

For blue native polyacrylamide gel electrophoresis (BN-PAGE), 75 μg of isolated mitochondria from the tibialis anterior muscle was incubated with digitonin extraction buffer [Hepes (30 mM), potassium acetate (150 mM), glycerol (12%), 6-aminocaproic acid (2 mM), EDTA (2 mM), and 6 g of high-purity digitonine per gram protein of mitochondria (pH 7.2)], and vortexed 1 hour at 4°C to solubilize membrane proteins. After incubation, solubilized extracts were centrifuged at 30,000g during 20 min, and supernatant are then mixed with loading dye [0.0125% (w/v) Coomassie Brilliant Blue G-250). Native complexes were resolved using bis-tris Invitrogen Novex NativePAGE 3 to 12% acrylamide gradient. OXPHOS complexes were visualized after in-gel activity (IGA) assays as described previously (*52*). Briefly, native gel was washed in potassium phosphate buffer (50 mM, pH 7.2) and then incubated in potassium phosphate buffer containing iodonitrotetrazolium (1 mg/ml), and NADH [400 μM (pH 7.2)] for Complex I. For Complex IV IGA assays, native gels were incubated in respiratory buffer [120 mM sucrose, 50 mM KCl, 20 mM tris-base, 4 mM KH_2PO_4, 2 mM MgCl2, and 1 mM EGTA (pH 7.2)] containing diaminobenzidine (1 mg/ml) and bovine cytochrome c (0.5 mg/ml). Coomassie staining was performed following the "PageBlue protein staining" (Fermentas) recommendations. BN-PAGE IGAs were collected using the Amersham ImageQuant 800 (GE Healthcare).

ATP synthase oligomerization

Three independent preparations of mitochondria isolated from the tibialis anterior muscle of 6-month-old WT and *Hacd1*-KO mice were resuspended at a protein concentration of 10 mg/ml in extraction buffer [150 mM potassium acetate, 15% (w/v) glycerol, 2 mM ε-amino caproic acid, and 30 mM Hepes (pH 7.4)] in the presence of protease inhibitors (Complete, Roche) and 1.5% digitonin (w/v). After an incubation of 30 min at 4°C, samples were centrifuged at

Downloaded from http://advances.sciencemag.org/ on January 26, 2021

25,000*g* for 30 min at 4°C. Ten microliters of supernatant was mixed with 1 μl of 0.0125% (w/v) SERVA blue G and loaded on 3 to 12% bis-tris native gel (Novex, Life Technologies). Anode buffer was prepared with a 20-fold dilution of Novex running buffer, and light blue cathode buffer was obtained by a 200-fold dilution of Novex cathode additive in anode buffer. Gels were run at 150 V for 120 min and ATPase activities were revealed in gel.

Measurement of fatty acid oxidation

Gastrocnemius muscles from 12-month-old mice were finely chopped in 2 ml of Krebs-Henseleit bicarbonate medium (pH 7.4) and then incubated in Erlenmeyer flasks containing a final volume of 25 ml of the same medium. Flasks were maintained at 37°C in an oxygenated atmosphere (O_2/CO_2, 95/5). For fatty acid oxidation determination, 1 pCi of ^{14}C-linoleate was added to the medium and the flask was hermetically sealed with rubber caps with centrally inserted plastic wells. After 20 to 30 min of incubation, 0.4 ml of 40% (w/v) $HClO_4$ was added through the rubber cap, and 0.4 ml of 1 M solution of hyamine hydroxide was deposed in the center of the well. The flasks were then shaked at room temperature for 1 hour. The radioactivity present in the center wells (corresponding to the formed CO_2) was determined and the flask content was harvested and centrifuged at 700*g* for 15 min. The resulting supernatant was neutralized with KOH (5 M), and total ^{14}C-labeled acid-soluble products were counted. Total fatty acid oxidation corresponded to the sum of the catabolism of labeled linoleate into CO_2 and acid-soluble products.

Mitoplast preparation

Freshly isolated mitochondrial pellets were incubated in 1 ml of H300 Mitoplast buffer [70 mM sucrose, 220 mM mannitol, and 2 mM Hepes (pH 7.4)] supplemented with 0.05% BSA and 0.12 μg of digitonin per microgram of mitochondrial protein, for 15 min at 4°C, with gentle shaking. Mitochondria were centrifuged at 8000*g* for 5 min and pellets were incubated in 1 ml of H40 Mitoplast buffer (H300 buffer diluted 7.5× in distilled water) for 15 min at 4°C, with gentle shaking. Suspension was then homogenized with a Dounce homogenizer (Sigma-Aldrich) and centrifuged at 8000*g* for 5 min. Pellets were resuspended in 1 ml of H40 buffer and centrifuged at 8000*g* for 5 min. Protein concentration was assessed using the bicinchoninic acid assay (Pierce).

Physical properties of mitochondrial membranes (TMA-DPH decay fluorescence)

TMA-DPH (Sigma-Aldrich) was used to monitor physical properties of mitochondrial membranes of 7- to 8-month-old mice. TMA-DPH is composed of a cationic substitute (TMA) that anchors at the polar heads of the membrane, while allowing the fluorescent hydrophobic probe DPH to be located in nonpolar regions. To limit fluorescent noise, mitoplasts were resuspended in the hypotonic buffer [9 mM sucrose, 29 mM mannitol, 0.3 mM Hepes (pH 7.4)] as described hereafter.

Experiments were repeated five times using independent samples, each from different mice. Decay-fluorescence measurements were performed on each sample at 37°C after a measurement of the instrumental response of the spectrofluorimeter used to measure fluorescence decay ("prompt"). Thirty microliters of sample [optical density $(OD)_{600}$ = 0.055] diluted in 2.97 ml of hypotonic buffer was introduced into spectroscopic quartz cuvette with an optical path length of 1 cm (VWR International).

Fluorescence decay was measured by the time-correlated single-photon counting (TCSPC) method using a Horiba-Fluoromax-4 spectrofluorimeter (Horiba) equipped with a 370-nm laser diode (NanoLED C2, Horiba) as the source of excitation. Fluorescence decays were measured in TCSPC setup (Deltahub, Horiba). The instrument response function was about 160 ps (measured at 370 nm using the hypotonic buffer). Emission and excitation wavelength of TMA-DPH were fixed at 370 nm and 431 ± 1.1 nm, respectively. Each decay curve corresponded to 10,000 counts.

Quantitative investigation of fluorescence decay of TMA-DPH

Curve smoothing

For illustration purposes, we smoothed the decay for the representative experiments using the generalized additive model of R statistical package "mgcv" with a Gaussian link and a *P*-spline smooth term. This smoothing was not used for the subsequent modeling steps below.

Finite exponential mixture model

We modeled the fluorescence decay obtained from the lipidomic analyses of mitoplasts using finite exponential mixtures (*28*). We accounted for the artifacts of the measuring apparatus by convolving the mixtures with the instrumental response (or "prompt"). The model was composed of 2*N* parameters, with *N* being the number of exponentials (each exponential has a scale and a characteristic time). We did not find it necessary to account for neither a potential time shift nor for background noise with an additional constant, as those additions did not improve the fit. More specifically, let $P(i)$ be the "prompt" (instrumental response) and $Y(i)$ the "decay" (experimental response) for channel i. The times of measurement are δi, with δ being the time interval between channels. The decay $G(t)$ at time t is given by a mixture of exponentials with characteristic times τk and scaling parameters Ck ($\mathcal{H}$ is the Heaviside function)

$$G(t) = \mathcal{H}(t) \sum_k C_k e^{-t/\tau_k}$$

Convolving with the prompt response $P(i)$ gives the model, with $Bk = \delta Ck$ scaling parameters

$$F(i) = \sum_{j=0}^{\infty} P(j)\, \mathcal{H}(t) \sum_k B_k e^{-\delta (i-j)/\tau_k}$$

For the optimization procedures, we reparametrized the τk to $\theta k = \log \tau k$.

Nonlinear mixed-effects models

To compare mixing proportions and characteristic times of decay, we used various nonlinear mixed-effects models (NLME) (see listing S1): first, a baseline NLME for the inner membrane that did not discriminate WT and *Hacd1*-KO (model A); second, two models where either the mixing proportions or the characteristic times of decay alone could vary between WT and *Hacd1*-KO (models B1 and B2, respectively); last, one model where both the mixing proportions and characteristic times were allowed to differ (model C).

More specifically, the mice phenotype (WT or *Hacd1*-KO) was encoded in a categorical factor with the following contrast matrix

$$L = \begin{pmatrix} & \textit{Hacd}1\text{-KO} & \text{WT} \\ \text{intercept} & 1 & 0 \\ \text{WT} & -1 & 1 \end{pmatrix}$$

For instance, the mean θ1 for population *Hacd1-KO* is the intercept, and the mean θ1 for population WT is (intercept) + (WT).

Downloaded from http://advances.sciencemag.org/ on January 26, 2021

Model fitting

We fitted the model through either a weighted nonlinear least-squares method at the experiment level or NLME with potential linear regressors for the fixed parameters.

Statistical analysis

For model comparison, we performed an analysis of variance (ANOVA), privileging the reading of the Akaike's information criterion (AIC) over that of the Bayesian information criterion and the *P* value of the log likelihood ratio (*53*).

Workflow

First, we determined the number of exponentials to use by comparing the AIC between potential models and whether models converged when fitted through a Levenberg-Marquardt nonlinear least-squares method. Then, we determined the appropriate random-effects structure and heteroscedasticity correction for NLME modeling by assessing convergence, AIC, within-experiment and between-experiment heteroscedasticity for various combinations. Last, we added a linear dependence of (some of) the fixed effects to a dummy variable WT/*Hacd1*-KO and assessed the statistical significance of this addition with an ANOVA.

Software implementation

The model is implemented in C++ using the Armadillo library for linear algebra and uses Armadillo's fast Fourier transform to perform the discrete convolution with the instrumental response. Both the optimization and analysis were made in the R statistical language with the package "nlme." All the codes are made available at github.com/ProlaLab/Prola2020.Sci.Adv with the appropriate tests and reproducible workflow (in addition, the releases are archived at https://doi.org/10.5281/zenodo.1228112). The raw data are available upon request at https://doi.org/10.5281/zenodo.4046133.

Lipidomic analyses

Mice (4 months old) were euthanized, and mitochondria were isolated from tibialis anterior muscles as described above and immediately frozen in liquid nitrogen and protected from oxidation by a layer of argon gas and stored at −80°C until analysis. Quantitation of fatty acids and glycerophospholipids contents was performed as previously described for myoblasts (*20*, *54*). Phospholipid species representation was performed as described hereafter. Briefly, total phospholipid amount was determined with Corona CAD detection by calculating the concentration of each phospholipid class (in microgram/ml) compared to calibration ranges of commercial standards. Chromatographic system from Thermo Fisher Scientific included a Dionex U-3000 Rapid Separation Liquid Chromatography (RSLC) system with two quaternary pumps, an autosampler, and a column oven. The RSLC system was coupled online to a charged aerosol detector, Corona-CAD Ultra for the quantitative part of the study and: a LTQ-Orbitrap Velos Pro for the lipidomic study (all from Thermo Fisher Scientific). Liquid chromatography, mass spectrometry, phospholipid species identification, and phospholipid species representation were performed as previously described (*55*). Statistical analysis was performed using multiple pairwise tests according to the Holm-Bonferroni method.

Mitochondrial phospholipids enrichment

Isolated mitochondria (500 µg) from 4-month-old mice were incubated in fusion buffer [220 mM mannitol, 70 mM sucrose, 2 mM Hepes, 10 mM KH_2PO_4, 5 mM $MgCl_2$, 1 mM EGTA, 10 mM glutamate, 2 mM malate, 10 mM pyruvate, and 2.5 mM ADP (pH 6.5)] for 20 min at 30°C under constant stirring agitation in the presence of 15 nmol of small unilamellar vesicles (SUVs), prepared as previously described (*56*), and using natural or fluorescent phospholipids (Avanti Polar Lipids). After fusion, mitochondria were layered on a sucrose gradient (0.6 M) and centrifuged 10 min at 10,000*g* at 4°C to remove SUV. Pellet was then washed in mitochondrial buffer 2 [250 mM sucrose, 3 mM EGTA, and 10 mM tris-HCl, (pH 7.4)]. Confocal images were acquired with a Zeiss LSM800 confocal (Zeiss).

NAO quantification

Isolated mitochondria or mitoplasts (100 µg of proteins) from 4-month-old mice were fixed in 2% formaldehyde for 15 min, centrifuged at 10,000*g* for 10 min and rinsed with PBS. The pellet was then resuspended and incubated 10 min at room temperature in 100 µl of PBS supplemented with 35 µM of NAO. Mitochondria or mitoplasts were then centrifuged at 10,000*g* for 10 min, and pellets were resuspended in 100 µl of PBS and fluorescence (λ excitation, 495 nm; λ emission, 620 nm) was acquired in 96-well plates with a spectrofluorimeter (TECAN infinite M200, TECAN, Austria).

Enzymatic assay

Complete enzymatic extractions from small pieces of frozen tissues from 4-month-old mice were obtained in an ice-cold buffer (1 ml for 50 mg of tissue) containing 5 mM Hepes (pH 8.7), 1 mM EGTA, 1 mM DTT, and 0.1% Triton X-100, using a Precellys homogenizer (Bertin), by two cycles of 8 s at 6500 rpm. Protein concentration was assessed using the bicinchoninic acid assay (Pierce). Total activity of COX and CS, were assayed at 30°C (pH 7.5), using standard spectrophotometric assays (*57*). Total activities of aconitase and fumarase were assayed from mitochondrial extracts at 30°C (pH 7.5), using standard spectrophotometric assays (*58*).

Protein carbonylation

Muscle carbonylation of proteins was quantified using the Oxyblot Protein Oxidation Detection Kit (Millipore). Briefly, protein lysates from the superficial gastrocnemius muscle of 4-month-old mice were prepared as for Western blots and treated to derivatize carbonyl groups according to the manufacturer's instructions. Then, protein extracts were separated by SDS-PAGE, transferred to a nitrocellulose membrane, and incubated with the provided primary and secondary antibodies. Light emission was recorded using a chemiluminescent detection system (G-Box, Syngene) and quantified by the ImageJ software (v1.47, NIH). Membrane was stained with Coomassie Blue, and protein content was normalized to one band.

Histological staining

Tibialis anterior muscles from 7-month-old mice were snap-frozen in isopentane cooled in liquid nitrogen and then stored at −80°C. Ten-micrometer-thick transverse sections were stained for glycerol-3-phosphate dehydrogenase (GPDH), succinate dehydrogenase (SDH), and NADH dehydrogenase (NADH tetrazolium reductase reaction, NADH-TR) activity as previously described (*59*). Livers were frozen in OCT embedding medium (Tissue-Tek). Ten-micrometer-thick transverse sections were fixed for 30 min in Baker solution (136 mM $CaCl_2$ and 4% HCHO), rinsed with water, and then stained with Oil Red O (ORO) solution (12 mM ORO in 70% ethanol) for 5 min (liver) or 30 min (muscle). The adipose tissue from gonadal pads was fixed in 10% formalin for 48 hours and embedded in paraffin. Four-micrometer-thick transverse sections were stained with

Downloaded from http://advances.sciencemag.org/ on January 26, 2021

hematoxylin-eosin. Images were captured using an Axio Observer Z1 microscope (Zeiss) and analyzed in a blinded manner using the ImageJ software (v1.47, NIH).

Electron microscopy

After euthanasia of 5- to 6-month-old mice, muscle tension and position were normalized by pinning the entire skinned hindlimb on a paraffin-coated dish, with the metatarsus making an angle of 90° with the tibia. The limb was then fixed with 2% glutaraldehyde in 0.1 M sodium cacodylate buffer (pH 7.2), at room temperature for 4 hours. Muscles were cut in small pieces and kept overnight in the same fixation buffer at 4°C. Samples were then processed at the Microscopy and Imaging Facility for Microbes, Animals and Foods MIMA2 platform, INRAE. They were contrasted with 0.5% oolong tea extract in cacodylate buffer, postfixed with a solution of 1% osmium tetroxide and 1.5% potassium cyanoferrate, and gradually dehydrated in ethanol (30 to 100%) and substituted gradually in a mix of propylene oxyde-epon and embedded in Epon (Delta microscopy). Thin sections (70 nm) were collected onto 200-mesh copper grids, and counterstained with lead citrate. Grids were examined with a Hitachi HT7700 electron microscope operating at 80 kV (Elexience). Images were acquired with a charge-coupled device camera (AMT).

Data analysis

For cristae quantification, 20 images at ×12,000 magnification were analyzed per animal, and all visible cristae were assessed using the function plot profile on ImageJ (v1.47, NIH). Mean cristae width corresponded to the maximal diameter of the tubular part and was calculated for each crista of each analyzed mitochondrion. For each animal, a minimum of 100 cristae was measured for the superficialis gastrocnemius muscle and 800 cristae for the soleus muscle. All images were analyzed in a blinded manner.

Fecal lipids quantitation

One gram of feces was collected after 8 weeks of HFD (7-month-old mice) and powdered using a tissue grinder. The powder was resuspended in 5 ml of normal saline solution (0.9% NaCl) and lipids were extracted in a mixture of chloroform:methanol (2:1). The solution was centrifuged at 1000*g* for 10 min. Lipids collected in the lower phase were air dried and weighted.

Quantification and statistical analysis

All data are presented as mean of values measured on distinct samples ± SE. Data were analyzed using Sigma Stat (Sigma Stat, version 3.0, Systat Software, San Jose, CA, USA). Raw data from each individual experiment were evaluated using an unpaired two-tailed *t* test with 95% confidence. For datasets that did not pass the D'Agostino and Pearson omnibus normality test (α, 0.05), differences were evaluated using a two-tailed unpaired nonparametric Mann-Whitney test with 95% confidence. Multiple pairwise tests were corrected using the Holm-Bonferroni method. The results of indirect calorimetry are expressed as mean ± SEM. Variance equality was analyzed by *F* test, and comparisons between groups were carried out using ANOVA with food (ND or HFD) or phase (day or night) and genotype of mice (WT or *Hacd1*-KO mice) and their interactions as factors followed by post hoc Tukey test. Data of calorimetrics presented represent mean of at least 96 hours measurement. Differences between groups were considered significant if the *P* value was less than 0.05.

Key resources

A complete set of the reagents used in this study is available in table S7.

SUPPLEMENTARY MATERIALS

Supplementary material for this article is available at http://advances.sciencemag.org/cgi/content/full/7/1/eabd6322/DC1

View/request a protocol for this paper from *Bio-protocol*.

REFERENCES AND NOTES

1. L. M. Jaacks, S. Vandevijvere, A. Pan, C. J. McGowan, C. Wallace, F. Imamura, D. Mozaffarian, B. Swinburn, M. Ezzati, The obesity transition: Stages of the global epidemic. *Lancet Diabetes Endocrinol.* **7**, 231–240 (2019).
2. J. Kerr, C. Anderson, S. M. Lippman, Physical activity, sedentary behaviour, diet, and cancer: An update and emerging new evidence. *Lancet Oncol.* **18**, e457–e471 (2017).
3. M. O. Goodarzi, Genetics of obesity: What genetic association studies have taught us about the biology of obesity and its complications. *Lancet Diabetes Endocrinol.* **6**, 223–236 (2018).
4. A. Chait, L. J. den Hartigh, Adipose tissue distribution, inflammation and its metabolic consequences, including diabetes and cardiovascular disease. *Front. Cardiovasc. Med.* **7**, 22 (2020).
5. D. A. Kass, P. Duggal, O. Cingolani, Obesity could shift severe COVID-19 disease to younger ages. *The Lancet* **395**, 1544–1545 (2020).
6. J. L. Kraschnewski, J. Boan, J. Esposito, N. E. Sherwood, E. B. Lehman, D. K. Kephart, C. N. Sciamanna, Long-term weight loss maintenance in the United States. *Int. J. Obes.* **34**, 1644–1654 (2010).
7. K. R. Westerterp, Physical activity, food intake, and body weight regulation: Insights from doubly labeled water studies. *Nutr. Rev.* **68**, 148–154 (2010).
8. Y.-H. Tseng, A. M. Cypess, C. R. Kahn, Cellular bioenergetics as a target for obesity therapy. *Nat. Rev. Drug Discov.* **9**, 465–482 (2010).
9. P. Mitchell, Coupling of phosphorylation to electron and hydrogen transfer by a chemi-osmotic type of mechanism. *Nature* **191**, 144–148 (1961).
10. S. Cogliati, J. A. Enriquez, L. Scorrano, Mitochondrial cristae: Where beauty meets functionality. *Trends Biochem. Sci.* **41**, 261–273 (2016).
11. N. Ikon, R. O. Ryan, Cardiolipin and mitochondrial cristae organization. *Biochim. Biophys. Acta Biomembr.* **1859**, 1156–1163 (2017).
12. G. Paradies, V. Paradies, V. De Benedictis, F. M. Ruggiero, G. Petrosillo, Functional role of cardiolipin in mitochondrial bioenergetics. *Biochim. Biophys. Acta* **1837**, 408–417 (2014).
13. M. Schlame, M. Ren, The role of cardiolipin in the structural organization of mitochondrial membranes. *Biochim. Biophys. Acta Biomembr.* **1788**, 2080–2083 (2009).
14. A. L. Duncan, A. J. Robinson, J. E. Walker, Cardiolipin binds selectively but transiently to conserved lysine residues in the rotor of metazoan ATP synthases. *Proc. Natl. Acad. Sci. U.S.A.* **113**, 8687–8692 (2016).
15. N. Ikon, R. O. Ryan, Barth syndrome: Connecting cardiolipin to cardiomyopathy. *Lipids* **52**, 99–108 (2017).
16. P. G. Barth, H. R. Scholte, J. A. Berden, J. M. V. D. K.-V. Moorsel, I. E. M. Luyt-Houwen, E. T. V. Veer-Korthof, J. J. V. D. Harten, M. A. Sobotka-Plojhar, An X-linked mitochondrial disease affecting cardiac muscle, skeletal muscle and neutrophil leucocytes. *J. Neurol. Sci.* **62**, 327–355 (1983).
17. V. Denic, J. S. Weissman, A molecular caliper mechanism for determining very long-chain fatty acid length. *Cell* **130**, 663–677 (2007).
18. T. Sassa, A. Kihara, Metabolism of very long-chain fatty acids: Genes and pathophysiology. *Biomol. Ther.* **22**, 83–92 (2014).
19. M. Ikeda, Y. Kanao, M. Yamanaka, H. Sakuraba, Y. Mizutani, Y. Igarashi, A. Kihara, Characterization of four mammalian 3-hydroxyacyl-CoA dehydratases involved in very long-chain fatty acid synthesis. *FEBS Lett.* **582**, 2435–2440 (2008).
20. J. Blondelle, Y. Ohno, V. Gache, S. Guyot, S. Storck, N. Blanchard-Gutton, I. Barthélémy, G. Walmsley, A. Rahier, S. Gadin, M. Maurer, L. Guillaud, A. Prola, A. Ferry, G. Aubin-Houzelstein, J. Demarquoy, F. Relaix, R. J. Piercy, S. Blot, A. Kihara, L. Tiret, F. Pilot-Storck, HACD1, a regulator of membrane composition and fluidity, promotes myoblast fusion and skeletal muscle growth. *J. Mol. Cell Biol.* **7**, 429–440 (2015).
21. E. Muhammad, O. Reish, Y. Ohno, T. Scheetz, A. DeLuca, C. Searby, M. Regev, L. Benyamini, Y. Fellig, A. Kihara, V. C. Sheffield, R. Parvari, Congenital myopathy is caused by mutation of HACD1. *Hum. Mol. Genet.* **22**, 5229–5236 (2013).
22. M. Pelé, L. Tiret, J.-L. Kessler, S. Blot, J.-J. Panthier, SINE exonic insertion in the PTPLA gene leads to multiple splicing defects and segregates with the autosomal recessive centronuclear myopathy in dogs. *Hum. Mol. Genet.* **14**, 1417–1427 (2005).
23. F. Al Amrani, C. Gorodetsky, L.-N. Hazrati, K. Amburgey, H. D. Gonorazky, J. J. Dowling, Biallelic LINE insertion mutation in *HACD1* causing congenital myopathy. *Neurol. Genet.* **6**, e423 (2020).

Downloaded from http://advances.sciencemag.org/ on January 26, 2021

24. H. Mi, A. Muruganujan, J. T. Casagrande, P. D. Thomas, Large-scale gene function analysis with the PANTHER classification system. *Nat. Protoc.* **8**, 1551–1566 (2013).
25. J. A. Mayr, V. Havlícková, F. Zimmermann, I. Magler, V. Kaplanová, P. Jesina, A. Pecinová, H. Nusková, J. Koch, W. Sperl, J. Houstek, Mitochondrial ATP synthase deficiency due to a mutation in the ATP5E gene for the F1 epsilon subunit. *Hum. Mol. Genet.* **19**, 3430–3439 (2010).
26. T. H. Haines, N. A. Dencher, Cardiolipin: A proton trap for oxidative phosphorylation. *FEBS Lett.* **528**, 35–39 (2002).
27. G. Oemer, K. Lackner, K. Muigg, G. Krumschnabel, K. Watschinger, S. Sailer, H. Lindner, E. Gnaiger, S. B. Wortmann, E. R. Werner, J. Zschocke, M. A. Keller, Molecular structural diversity of mitochondrial cardiolipins. *Proc. Natl. Acad. Sci.* **115**, 4158–4163 (2018).
28. C. D. Stubbs, C. Ho, S. J. Slater, Fluorescence techniques for probing water penetration into lipid bilayers. *J. Fluoresc.* **5**, 19–28 (1995).
29. H. Schneider, J. J. Lemasters, M. Höchli, C. R. Hackenbrock, Liposome-mitochondrial inner membrane fusion. Lateral diffusion of integral electron transfer components. *J. Biol. Chem.* **255**, 3748–3756 (1980).
30. J. Grundlingh, P. I. Dargan, M. El-Zanfaly, D. M. Wood, 2,4-Dinitrophenol (DNP): A weight loss agent with significant acute toxicity and risk of death. *J. Med. Toxicol.* **7**, 205–212 (2011).
31. R. J. Perry, D. Zhang, X.-M. Zhang, J. L. Boyer, G. I. Shulman, Controlled-release mitochondrial protonophore reverses diabetes and steatohepatitis in rats. *Science* **347**, 1253–1256 (2015).
32. B. Wang, J. Pelletier, M. J. Massaad, A. Herscovics, G. C. Shore, The yeast split-ubiquitin membrane protein two-hybrid screen identifies BAP31 as a regulator of the turnover of endoplasmic reticulum-associated protein tyrosine phosphatase-like B. *Mol. Cell. Biol.* **24**, 2767–2778 (2004).
33. D. Acehan, A. Malhotra, Y. Xu, M. Ren, D. L. Stokes, M. Schlame, Cardiolipin affects the supramolecular organization of ATP synthase in mitochondria. *Biophys. J.* **100**, 2184–2192 (2011).
34. M. Zhang, E. Mileykovskaya, W. Dowhan, Cardiolipin is essential for organization of complexes III and IV into a supercomplex in intact yeast mitochondria. *J. Biol. Chem.* **280**, 29403–29408 (2005).
35. S. E. Gasanov, A. A. Kim, L. S. Yaguzhinsky, R. K. Dagda, Non-bilayer structures in mitochondrial membranes regulate ATP synthase activity. *Biochim. Biophys. Acta Biomembr.* **1860**, 586–599 (2018).
36. D. A. Cherepanov, W. Junge, A. Y. Mulkidjanian, Proton transfer dynamics at the membrane/water interface: Dependence on the fixed and mobile pH buffers, on the size and form of membrane particles, and on the interfacial potential barrier. *Biophys. J.* **86**, 665–680 (2004).
37. C. Zhang, D. G. Knyazev, Y. A. Vereshaga, E. Ippoliti, T. H. Nguyen, P. Carloni, P. Pohl, Water at hydrophobic interfaces delays proton surface-to-bulk transfer and provides a pathway for lateral proton diffusion. *Proc. Natl. Acad. Sci. U.S.A.* **109**, 9744–9749 (2012).
38. T. Nilsson, C. R. Lundin, G. Nordlund, P. Ädelroth, C. von Ballmoos, P. Brzezinski, Lipid-mediated protein-protein interactions modulate respiration-driven ATP synthesis. *Sci. Rep.* **6**, 24113 (2016).
39. A. Toth, A. Meyrat, S. Stoldt, R. Santiago, D. Wenzel, S. Jakobs, C. von Ballmoos, M. Ott, Kinetic coupling of the respiratory chain with ATP synthase, but not proton gradients, drives ATP production in cristae membranes. *Proc. Natl. Acad. Sci. U.S.A.* **117**, 2412–2421 (2020).
40. M. Y. Yoshinaga, M. Y. Kellermann, D. L. Valentine, R. C. Valentine, Phospholipids and glycolipids mediate proton containment and circulation along the surface of energy-transducing membranes. *Prog. Lipid Res.* **64**, 1–15 (2016).
41. A. Mühleip, S. E. McComas, A. Amunts, Structure of a mitochondrial ATP synthase with bound native cardiolipin. *eLife* **8**, (2019).
42. G. F. Azzone, T. Pozzan, E. Viola, P. Arslan, Proton electrochemical gradient and phosphate potential in submitochondrial particles. *Biochim. Biophys. Acta Bioenerg.* **501**, 317–329 (1978).
43. P. Mitchell, A commentary on alternative hypotheses of protonic coupling in the membrane systems catalysing oxidative and photosynthetic phosphorylation. *FEBS Lett.* **78**, 1–20 (1977).
44. B. Rieger, W. Junge, K. B. Busch, Lateral pH gradient between OXPHOS complex IV and F 0 F 1 ATP-synthase in folded mitochondrial membranes. *Nat. Commun.* **5**, 1–7 (2014).
45. A. Joly-Amado, R. G. P. Denis, J. Castel, A. Lacombe, C. Cansell, C. Rouch, N. Kassis, J. Dairou, P. D. Cani, R. Ventura-Clapier, A. Prola, M. Flamment, F. Foufelle, C. Magnan, S. Luquet, Hypothalamic AgRP-neurons control peripheral substrate utilization and nutrient partitioning. *EMBO J.* **31**, 4276–4288 (2012).
46. M. D. Bruss, C. F. Khambatta, M. A. Ruby, I. Aggarwal, M. K. Hellerstein, Calorie restriction increases fatty acid synthesis and whole body fat oxidation rates. *Am. J. Physiol. Endocrinol. Metab.* **298**, E108–E116 (2010).
47. G. Derumeaux, F. Ichinose, M. J. Raher, J. G. Morgan, T. Coman, C. Lee, J. M. Cuesta, H. Thibault, K. D. Bloch, M. H. Picard, M. Scherrer-Crosbie, Myocardial alterations in senescent mice and effect of exercise training: A strain rate imaging study. *Circ. Cardiovasc. Imaging* **1**, 227–234 (2008).
48. V. Ferferieva, A. Van den Bergh, P. Claus, R. Jasaityte, A. La Gerche, F. Rademakers, P. Herijgers, J. D'hooge, Assessment of strain and strain rate by two-dimensional speckle tracking in mice: Comparison with tissue Doppler echocardiography and conductance catheter measurements. *Eur. Heart J. Cardiovasc. Imaging* **14**, 765–773 (2013).
49. J. Vandesompele, K. De Preter, F. Pattyn, B. Poppe, N. Van Roy, A. De Paepe, F. Speleman, Accurate normalization of real-time quantitative RT-PCR data by geometric averaging of multiple internal control genes. *Genome Biol.* **3**, RESEARCH0034 (2002).
50. A. Mourier, B. Ruzzenente, T. Brandt, W. Kühlbrandt, N.-G. Larsson, Loss of LRPPRC causes ATP synthase deficiency. *Hum. Mol. Genet.* **23**, 2580–2592 (2014).
51. A. V. Kuznetsov, V. Veksler, F. N. Gellerich, V. Saks, R. Margreiter, W. S. Kunz, Analysis of mitochondrial function in situ in permeabilized muscle fibers, tissues and cells. *Nat. Protoc.* **3**, 965–976 (2008).
52. I. Wittig, H.-P. Braun, H. Schägger, Blue native PAGE. *Nat. Protoc.* **1**, 418–428 (2006).
53. K. P. Burnham, D. R. Anderson, *Model Selection and Multimodel Inference - A Practical* (Springer-Verlag New York, New York, 2002); http://www.springer.com/us/book/9780387953649.
54. J. Blondelle, J.-P. Pais de Barros, F. Pilot-Storck, L. Tiret, Skeletal muscle development, in *Methods in Molecular Biology*, J. Ryall, Ed. (Springer, 2017), vol. 1668, pp. 39–60.
55. M. Moulin, A. Solgadi, V. Veksler, A. Garnier, R. Ventura-Clapier, P. Chaminade, Sex-specific cardiac cardiolipin remodelling after doxorubicin treatment. *Biol. Sex Differ.* **6**, 20 (2015).
56. R. Mendez, S. Banerjee, Sonication-based basic protocol for liposome synthesis. *Methods Mol. Biol.* **1609**, 255–260 (2017).
57. F. Caffin, A. Prola, J. Piquereau, M. Novotova, D. David, A. Garnier, D. Fortin, M. Alavi, V. Veksler, R. Ventura-Clapier, F. Joubert, Altered skeletal muscle mitochondrial biogenesis but improved endurance capacity in trained OPA1-deficient mice. *J. Physiol.* **591**, 6017–6037 (2013).
58. J. Piquereau, F. Caffin, M. Novotova, A. Prola, A. Garnier, P. Mateo, D. Fortin, L. H. Huynh, V. Nicolas, M. V. Alavi, C. Brenner, R. Ventura-Clapier, V. Veksler, F. Joubert, Down-regulation of OPA1 alters mouse mitochondrial morphology, PTP function, and cardiac adaptation to pressure overload. *Cardiovasc. Res.* **94**, 408–417 (2012).
59. G. L. Walmsley, S. Blot, K. Venner, C. Sewry, J. Laporte, J. Blondelle, I. Barthélémy, M. Maurer, N. Blanchard-Gutton, F. Pilot-Storck, L. Tiret, R. J. Piercy, Progressive structural defects in canine centronuclear myopathy indicate a role for HACD1 in maintaining skeletal muscle membrane systems. *Am. J. Pathol.* **187**, 441–456 (2017).

Acknowledgments: We are grateful to C. Laisne and D. Gelperowic for taking care of mice; J.-P. Pais de Barros and the LAP platform (Dijon, France) for lipidomic analyses; C. Longin and M. Letheule for electron microscopy (Microscopy and Imaging Facility for Microbes, Animals and Foods MIMA2 platform, INRAE, Jouy-en-Josas, France); G. Delahaye, M.-P. Sellier, and C. Poncet for technical help; R. Ventura-Clapier for insightful discussions; and G. Walmsley for the edition of an interim version of the manuscript. We acknowledge the technical platform of metabolism of the Unit "Biologie Fonctionnelle et Adaptative" (University de Paris, BFA, UMR 8251 CNRS, Paris, France) for metabolic analysis and the animal core facility "Buffon" of the Université de Paris–Institut Jacques Monod for animal husbandry and the Plateau Technique d'IMagerie Spectroscopique (PIMS), which is a part of DImaCell platform (Université de Bourgogne–INRAE, Dijon, France). **Funding:** N.Kh.'s Ph.D. fellowship has been financially supported by the French "Fondation pour la Recherche Médicale" (FRM). The work was primarily supported by the French "Agence Nationale de la Recherche" (ANR-12-JSV1-0005) and the "Association Française contre les Myopathies" (AFM #16143, Translamuscle I #19507, and Translamuscle II #22946). **Author contributions:** Conceptualization, A.P., J.B., and F.P.-S.; methodology, A.P., S.G., A.S., N.Ko., G.D., M-F.G., F.J., S.L., and F.P.-S.; formal analysis, A.P., J.B., A.V., J.P., R.G.P.D., S.G., A.Ma., M.M., C.H., N.Kh., C.G., T.M., G.C., L.G., M.G., A.S., J.C., J.T., J.D., A.Mo., G.D., and F.P.-S.; data curation, A.P., J.B., J.P., R.G.P.D., S.G., H.C., A.Ma., C.H., A.S., F.D., J.D., A.Mo., N.Ko., G.D., M-F.G., V.V., S.L., and F.P.-S.; figures conception, A.P., J.B., R.G.P.D., H.C., A.Mo., L.T., and F.P.-S.; writing, original draft, A.P., L.T., and F.P.-S.; review and editing, all authors; funding acquisition, F.R., L.T., and F.P.-S.; resources, J.P., R.G.P.D., S.G., H.C., A.Ma., J.D., A.Mo., N.Ko., M.-F.G., F.J., V.V., S.L., F.R., L.T., and F.P.-S.; supervision, A.P., F.R., L.T., and F.P.-S. **Competing interests:** The authors declare that they have no competing interests. **Data materials and availability:** All data needed to evaluate the conclusions in the paper are present in the paper and/or the Supplementary Materials. Additional data related to this paper may be requested from F.P.-S. (fanny.storck@vet-alfort.fr).

Submitted 8 July 2020
Accepted 4 November 2020
Published 1 January 2021
10.1126/sciadv.abd6322

Citation: A. Prola, J. Blondelle, A. Vandestienne, J. Piquereau, R. G. P. Denis, S. Guyot, H. Chauvin, A. Mourier, M. Maurer, C. Henry, N. Khadhraoui, C. Gallerne, T. Molinié, G. Courtin, L. Guillaud, M. Gressette, A. Solgadi, F. Dumont, J. Castel, J. Ternacle, J. Demarquoy, A. Malgoyre, N. Koulmann, G. Derumeaux, M.-F. Giraud, F. Joubert, V. Veksler, S. Luquet, F. Relaix, L. Tiret, F. Pilot-Storck, Cardiolipin content controls mitochondrial coupling and energetic efficiency in muscle. *Sci. Adv.* **7**, eabd6322 (2021).

Downloaded from http://advances.sciencemag.org/ on January 26, 2021

Science Advances

Cardiolipin content controls mitochondrial coupling and energetic efficiency in muscle

Alexandre Prola, Jordan Blondelle, Aymeline Vandestienne, Jérôme Piquereau, Raphaël G. P. Denis, Stéphane Guyot, Hadrien Chauvin, Arnaud Mourier, Marie Maurer, Céline Henry, Nahed Khadhraoui, Cindy Gallerne, Thibaut Molinié, Guillaume Courtin, Laurent Guillaud, Mélanie Gressette, Audrey Solgadi, Florent Dumont, Julien Castel, Julien Ternacle, Jean Demarquoy, Alexandra Malgoyre, Nathalie Koulmann, Geneviève Derumeaux, Marie-France Giraud, Frédéric Joubert, Vladimir Veksler, Serge Luquet, Frédéric Relaix, Laurent Tiret and Fanny Pilot-Storck

Sci Adv **7** (1), eabd6322.
DOI: 10.1126/sciadv.abd6322

ARTICLE TOOLS http://advances.sciencemag.org/content/7/1/eabd6322

SUPPLEMENTARY MATERIALS http://advances.sciencemag.org/content/suppl/2020/12/21/7.1.eabd6322.DC1

REFERENCES This article cites 56 articles, 11 of which you can access for free
http://advances.sciencemag.org/content/7/1/eabd6322#BIBL

PERMISSIONS http://www.sciencemag.org/help/reprints-and-permissions

Use of this article is subject to the Terms of Service

Science Advances (ISSN 2375-2548) is published by the American Association for the Advancement of Science, 1200 New York Avenue NW, Washington, DC 20005. The title *Science Advances* is a registered trademark of AAAS.

Copyright © 2021 The Authors, some rights reserved; exclusive licensee American Association for the Advancement of Science. No claim to original U.S. Government Works. Distributed under a Creative Commons Attribution NonCommercial License 4.0 (CC BY-NC).

Downloaded from http://advances.sciencemag.org/ on January 26, 2021